Experimental investigation of walking drops: Wave field and interaction with slit structures

Clive Ellegaard and Mogens T. Levinsen [*]

Niels Bohr Institute, University of Copenhagen, Blegdamsvej 17, DK-2100 Copenhagen Ø, Denmark

While bouncing walking silicone oil droplets (walkers) do show many quantumlike phenomena, the original, most intriguing, double-slit experiment with walkers has been shown to be an overinterpretation of data. Several experiments and numerical simulations have proven that for at least some parameter region there is no randomness. Still, true randomness was claimed to be observed in an experiment on chaotically bouncing walkers. Also, most of the available phase space has not been investigated. The main goal of this paper is therefore to look for true interference and chaos in the entire phase space. Recently, we made an extensive investigation of drops interacting with slits, but still in a limited range. However, the outcome was always deterministic and only incidentally mimicked the statistics of the corresponding quantum case. We also showed that the extra interference, already seen by others, in the double-slit case was caused by reflection of waves from the outlet of the unused slit after passage and thus was not a true double-slit effect. A new theoretical treatment of bouncing drop dynamics has since given analytic relations for the associated wave field, leading to a proposal for criteria for the possible occurrence of true interference in the double-slit experiment. Satisfying these criteria, requires working close to the onset of the Faraday instability, with two spatial conditions favoring slow walkers, and a temporal condition favoring fast walkers. The regions of high velocity, where the walkers bounce periodically, and of very low velocity, with chaotically bouncing walkers, have not been comprehensively investigated so far. We have therefore looked at these regions, probing the limits for interaction with slits. Furthermore, noting that a short transit time is essential to fulfill the criteria, experiments were done using double-slit barriers only 0.5 and 2 mm broad. Nowhere was true interference or a chaotic response found. As the theory has implications for many of the observed quantumlike phenomena involving walkers as, e.g., tunneling and interaction between drops, we have measured the spatial and temporal decay of the wave field. A comparison with the theory shows very good agreement but leads to a reformulation of the above-mentioned criteria.

I. INTRODUCTION

Oil drops on a vibrated surface of the same oil will, under the right conditions, turn into "walkers" as shown by Couder *et al.* in Ref. [1]. In that paper the authors also show the first quantumlike phenomenon: Two drops on the same surface will interact through their wave fields and move in circles around each other. These circles turn out to have quantized radii.

Shortly after this, in 2006, Couder and Fort [2] published their truly intriguing paper on walkers diffracted by submerged single- and double-slit barriers and apparently satisfying the same statistics as true Quantum Systems. This triggered the emergence of a new field of hydrodynamic quantum analogs, which apart from diffraction experiments [3–7], has touched on subjects such as, e.g., quantization of bound states in two-body interactions [8,9], the quantum harmonic oscillator [10,11], tunneling [12–14], the quantum corral [15–18], and scattering [19]. For a recent thorough review of the field, see Ref. [20].

Previous investigations on the diffraction experiment were centered on examining the validity of the observation by Couder and Fort [2] concerning the quantumlike statistics, and mostly operated in the regime of slow moving chaotically bouncing droplets (see Fig. 1). Andersen *et al.* [3] were unable to reproduce the quantumlike statistics and also pointed out problems with the statistical uncertainty due to the low number of walkers involved. However, they did observe that an extra interference effect was present for the double-slit. This was confirmed by Pucci *et al.* [6] who in addition found a deterministic outcome for a wide slit structure although in a rather limited part of the possible parameter space for chaotically bouncing walkers (see Fig. 1(a), Ref. [6], and Fig. 1, this paper). They also reported a chaotic outcome at drive levels extremely close to the onset of spontaneously excited Faraday waves [21].

A large part, marked by the orange hatched region in Fig. 1, of the available parameter space at high drive levels involving chaotically bouncing walkers were covered systematically by Ellegaard and Levinsen [7]. This investigation examined both single- and double-slits of several slit sizes, and revealed a rich scenario of interferencelike patterns. However, the outcome was always deterministic with the chaotic scenario reported by Pucci *et al.* [6] shown to be a result of response patterns rapidly changing with drive amplitude and therefore not related to chaos (see Figs. 10 and 19 in Ref. [7]). Furthermore, we were able to show unambiguously that the extra

----

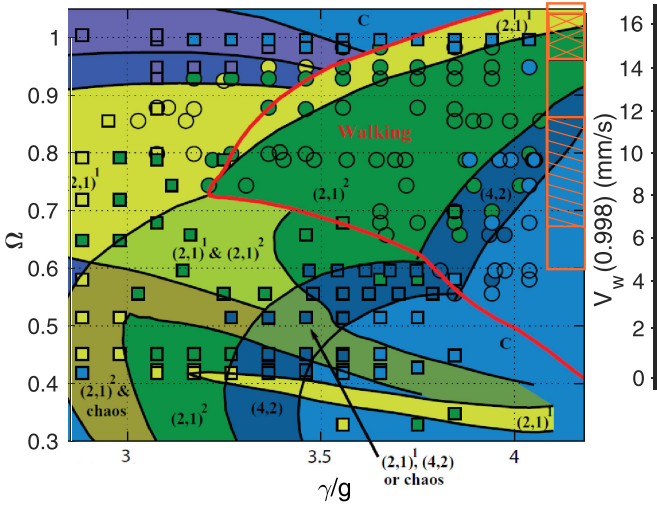[*]levinsen@nbi.dk

FIG. 1. Part of (Ω, γ) parameter space, reproduced from Wind-Willassen *et al.* [Phys. Fluids **25**, 082002 (2013)], Fig. 3(a), with the permission of AIP Publishing, and augmented with a V_w y axis. Note that this axis refers to the velocity V_w of the drop at $\gamma/\gamma_F = 0.998$, where γ and γ_F are the drive and the critical drive, respectively. Ω is the vibration number of the drop (for definitions, see Table I). The region of interest is the walker region limited to the left by the red borderline. The notation $(m, n)^q$ refers to the periodicity of the bouncing where m is the number of driving periods and n is the number of contacts with the bath with the superscript q distinguishing different phase-shifted modes. The squares denote stationary bouncers while the circles denote walkers, with the colors denoting the associated $(m, n)^q$ state. In the light blue area marked "C" the walkers bounce chaotically. The small orange hatched rectangle to the right shows the area covered by previous investigations, while the large (orange-bordered) rectangle shows the total phase space now covered in detail by our investigations. The orange cross-hatched rectangle denotes a transition zone (see Sec. IV B).

interference is solely due to the wave structure generated after passage interacting with the backside of the unused slit. Thus, it is *not* a true double-slit interference effect.

The landscape that the drop is moving in is best illustrated by Fig. 1. In this figure, extracted and adapted from Fig. 3(a) of Ref. [22], the (Ω, γ) parameter space for walkers is displayed. For ease of comparison with the experimental results we have supplied the figure with an additional y axis to the right, showing the approximate free space velocity $V_w(0.998)$ of the drop at $\gamma/\gamma_F = 0.998$ that corresponds to Ω. (For definitions, see Fig. 1 and Table I.)

Our previous investigation only involved drop velocities, V_w, between 6.4 mm/s and 12 mm/s. This region is represented by the small orange hatched rectangle to the right in Fig. 1 limited by those velocities. Other prior investigations are also inside this regime [3,6,23]. This means that less than half of the available phase space for walkers at high drive levels has ever been thoroughly examined.

Thus, the foremost aim of this investigation is as follows. To make a thorough investigation of the full available phase space for walkers with the aim of observing, first, whether true interference can be obtained, and second, whether chaotic dynamics can lead to quantumlike behavior.

Since the first experiment by Couder and Fort [2] several theoretical papers have examined the interaction between walking droplets and submerged barriers [24–26]. More recently Tadrist *et al.* [27] analytically derived relations describing the wave field accompanying the walker.

Their theory has implications for many of the quantum analogs observed including the diffraction experiments, and has also already been used to choose the parameters for a tunneling experiment [14]. We therefore consider it of broad interest to experimentally investigate the extent of the validity of the theory. This was only checked by the authors up to $M = 50$, where M is the memory factor given by $M = \gamma_F/(\gamma_F - \gamma)$.

To assess the possibility for real interference in the double-slit experiment, knowledge of the spatial and temporal decay of the wave field is needed. On the basis of their theory Tadrist *et al.* [27] developed some simple criteria concerning this. The spatial criteria $l(0)_D = l(0)/l_{ch} \gg 1$ and $R/l(0) \gg 1$ compare the decay length, l, of the field in front of the drop with a characteristic length $l_{ch} = \sqrt{2}d = \sqrt{2}(L + L_b)$ and with the inner radius, R, of the container (see Table I and Fig. 2 for definitions). The temporal criterion $\tau_D = \tau_M/T_{ch} \gg 1$ likewise compares the decay time of the memory of the field, τ_M, with a characteristic traveling time $T_{ch} = l_{ch}/V_w$.

In Sec. II we describe some of the more important general experimental details. This is followed by a presentation of the theory by Tadrist *et al.* [27] on the wave field accompanying the walker in Sec. III A.

In the rest of the paper we present our new experimental results. In Sec. III B we treat the measurements on the spatial extent and the temporal memory of the wave field. As the highest possible values of M are necessary for the criteria to hold, we have measured the decay length and decay time up to $M = 500$. These measurements show excellent agreement with the full theory. Noting discrepancies with approximations used in the development of the criteria, we reformulate these using the full theory. The reformulated criteria are then used to identify areas of interest in the search for true interference effects.

This has led us to make new measurements in both the very low velocity regime (Sec. IV A) and the high velocity regime (Sec. IV B and Appendix A). Together with the measurements described in Ref. [7] these measurements constitute a full coverage of the available phase space for single-slits of width L of order 5 to 14.7 mm and double-slits between $L = 5$ and 7.5 mm. In Fig. 1 the phase space now covered is represented by the large orange bordered rectangle stretching from $V_w(0.998) = 4.9$ to 17 mm/s.

In practice the criteria are impossible to satisfy. However, they can be met to such a degree that some vestiges of true interference ought to be observable making the attempt seem worthwhile. This search also involved looking carefully for traces of chaotic dynamics in single-slits with L between 5.2 and 14.7 mm.

A major advance in our attempts is in the use of ultra-thin barriers. As stated the criteria ignore the breadth, b, of the barrier (see Fig. 2). In doing so, they highlight a problem inherent in all prior experiments, where a significant delay strongly dependent on x_{imp} was caused by the time spent in the slit. In the meantime the wave field passing through the other

TABLE I. Table of notation for some important parameters. See Figs. 2 and 6 for more information.

| Container (see Fig. 2)			
Radius, deep section	$R = 90$ mm	Center block	$L_b = 4.7$ mm
Height of barrier, accelerator, shelf	5 mm	barrier breadth	b: 5, 2, 0.5 mm
Slit opening	L: 14.7, 7.5, 7.3, 5.2 mm	Double slit	$d = L + L_b$
Fluid			
Density	$\rho = 950$ kg/m^3	Surface tension	$\sigma = 0.0206$ N/m
Viscosity	$\nu = 20$ mPa s	Diffusion coefficient	$D_{\text{diff}} = 2.20$ mm^2
Fluid height	h	Height over barrier	h_1
Surface elevation	$\zeta(\mathbf{r}, t)$	Envelope Field	$\eta(\mathbf{r}, t)$
Viscous boundary layer	$\delta = \sqrt{(2\nu/2\pi f)}$		
Drive			
Frequency	$f = 80$ Hz	Amplitude	γ
Normalized time:	$\tau = (\pi f/2)t$		
Faraday			
Period	$T_F = 2/f$	Wavelength	$\lambda_F = 4.75$ mm
Wave number	k_F	Threshold	γ_F
Free damping	$\gamma_0 = 0.277$		
Drop			
Drop diameter	D	Vibration number	$\Omega = 2\pi f \sqrt{\rho D^3/(8\sigma)}$
Impact phase	τ_i	Previous impacts	τ_n
Drop velocity	V_w	Normalized	$v = V_w/\pi f$
Impact parameter	x_{imp} (see Fig. 2)	deflection angle	α (see Fig. 2)
Memory factor	$M = \gamma_F/(\gamma_F - \gamma)$	Memory number	$M_e \approx 0.76M$
Characteristic length	$l_{\text{ch}} = \sqrt{2}d$	Characteristic time	$T_{\text{ch}} = l_{\text{ch}}/V_w$
Damping time	$\tau_M = M_e T_F$	Normalized	$\tau_D = \tau_M/T_{\text{ch}}$
Damping length	$l(\Theta)$	Normalized	$l(\Theta)_D = l(\Theta)/l_{\text{ch}}$
Damping length defined by 3% contour	$l^*(\Theta)$ (see Fig. 6)	Normalized	$l^*(\Theta)_D = l^*(\Theta)/l_{\text{ch}}$
Angle between velocity vector and $\mathbf{r}$	Θ (see Fig. 6)	Low velocity limit	V_{low}
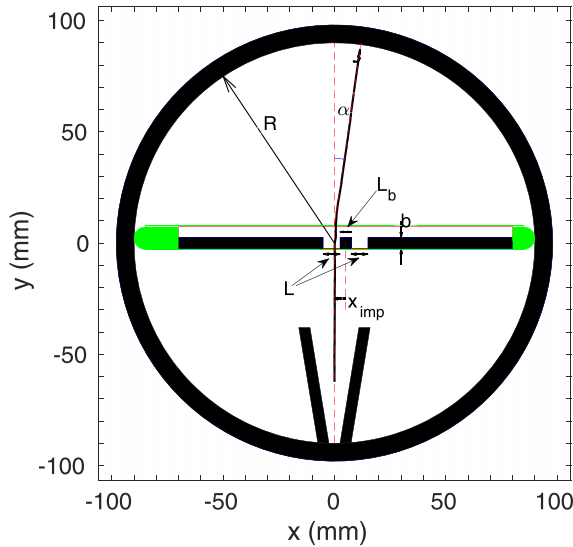
FIG. 2. Top view of the interior of the container with a double-slit of slit width, L, and breadth, b, inserted in a groove, the free ends of which is shown in green. The radius of the free surface of the oil is 97 mm while the radius, R, of the deep section (white) is 90 mm. The black parts all have the height 5 mm. The width, L_b, of the central block is always 4.7 mm, while L and b can vary. A single trajectory is shown to allow for the definitions of the deflection angle α and the impact parameter x_{imp}.

slit is slowly deteriorating. We have minimized this delay in double-slit experiments where b is only 0.5 mm, respectively, 2 mm. These new measurements are treated in Sec. IV C. In doing this we have again searched the whole available phase space while also using single-slit barriers to look for possible chaotic outcomes.

During the investigation we observed that the window in x_{imp} giving free passage became reduced and even split up at high velocities. At even higher velocities no free passage was allowed. Here the impact parameter x_{imp} is defined in Fig. 2. This phenomenon is explored in Sec. IV B and Appendix A. Thus, the velocity phase space for passing on beyond the barrier is bounded from above as well as from below [6,7].

II. EXPERIMENTAL DETAILS

The most important experimental features will be presented in this section, but a full account of the experimental details can be found in Ref. [7]. A top view of the interior of the container is shown in Fig. 2 and includes definitions of several important parameters. The deep part of the container of radius $R = 90$ mm is surrounded by a 5 mm high and 7 mm broad shelf that dampens reflections of waves from the outer rim. Barriers, movable from outside by a step-motor during the experiment, are placed in a central groove. A built-in accelerator, the V-shape, ends 3.8 cm before the slit system.

Both barriers and accelerator have the same height of 5 mm as the shelf. The $b = 5$ mm single- and double-slit barriers used have slit opening L equal to 5.2, 7.3, 7.5, or 14.7 mm. The $b = 2$ mm double-slit barrier has $L = 5.2$ mm, while the $b = 0.5$ mm single-slit has $L = 5.2$ mm and the double-slits have either $L = 5.2$ mm or $L = 7.3$ mm. The central block of all double-slit barriers have a width of $L_b = 4.7$ mm. The uncertainty on all these quantities, including the distance d between the slit centers, is less than 0.1 mm.

The definitions of the impact parameter x_{imp} (lateral distance from the center of the slit system to the center of the accelerator) and the deflection angle α are also shown in Fig. 2. The uncertainties on these parameters are $\pm$ 0.2 mm and $\pm 0.3°$, respectively.

A glass lid resting on a transparent plastic cylinder closes the container hermetically to avoid air movement in the cell to disturb the drops. However, slow diffusive pressure equalization is provided for by a porous plug. A horizontal drops-on-command cannon enters the side of the plastic cylinder through a hole sealed with a rubber membrane. Drop size and consequently drop velocity can be easily chosen by selection of the height and duration of the voltage pulse supplied to the piezo electric actuator of the cannon. The experiment is controlled by a homemade LabView program that also records the frequency f of the drive, a range of relevant accelerations and temperatures, besides the starting point of the drop on the surface. A Matlab program controls the ccd camera and a second Matlab program records the drop trajectories with both programs controlled by the LabView program. Taken together with the movable barrier, this arrangement ensures that the data collection can be automated to collect large amounts of trajectories without opening the container system.

Strict temperature control of the system is very important, as explained in detail in Ref. [7]. Therefore, we keep the temperature of the oil at nominally 25 °C and within a relative uncertainty of $\pm$ 0.005 °C, which for the silicone oil of nominal viscosity $\nu = 20$ mPa s means, that all measurements are performed at a frequency of $f = 80$ Hz. Equally important, the accelerometer is also temperature stabilized. Thus, we have a statistical uncertainty on the drive amplitude, γ, of less than 0.03% while the uncertainty on the critical amplitude γ_F is dominated by a systematic error of less than 0.06%. The measured wavelength λ_F of the Faraday waves is approximately 4.8 mm.

A new addition to our setup consists of a retractable system consisting of a horizontally mounted second camera that together with a mirror set at $45°$ gives a top view of the drop. An LED light is synchronized to the drive. Using a pulse length of 0.2 ms, we have re-calibrated the drop diameter D. This showed that our previous calibration was off by between 4 and 9% (footnote [28]) depending on V_w. One feature of this setup is that we can actually distinguish between simple modes of bouncing.

III. WAVEFORM: THEORY AND EXPERIMENTS

A. Theory

In the following we shall go through some of the elements of the theory by Tadrist *et al.* [27]. In doing this, we pay spe-

cial attention to the assumptions made during the derivation, so they can be subjected to an experimental check.

To describe the dynamics of the walkers it is necessary to understand the interaction with the Faraday capillary surface waves. Thus, any theory for the walkers must build on the theory for these waves. Since Faraday [21] first observed the spontaneous emergence of waves on a vibrated fluid surface, substantial efforts have gone into developing a theory describing this phenomenon. Benjamin and Ursell [29] showed that the equation for the surface elevation $\zeta(x, y, t)$ could be written as a Mathieu equation when the fluid is inviscid and the depth of the fluid infinite,

$$\frac{d^2\zeta}{dt^2} = gk + \frac{\sigma}{\rho}k^3 - \gamma gk\cos(2\pi ft). \tag{1}$$

Here k is the wave number. This equation has as solution a subharmonic resonance with wavelength $\lambda_F = 2\pi/k_F$ at k_F given by

$$(2\pi f/2)^2 = gk_F + \frac{\sigma}{\rho}k_F^3. \tag{2}$$

However, the parametric instability thus occurring at half the drive frequency has a threshold of zero due to the fluid being inviscid, which of course is unphysical.

Several attempts have been made to remedy this situation by inserting a phenomenological damping term, e.g., Refs. [30–32]. However, these all assume that the viscous damping is small and that the Faraday waves are in phase with the drive. None of these assumptions are in fact correct.

Without any restrictions on viscosity and fluid depth, Kumar and Tuckerman [33] solved the full linearized Navier-Stokes equations in the presence of parametric forcing by using a Floquet analysis. However, due to the parametric forcing the result is given as an infinite system of coupled equations for the Fourier modes. By truncating the Fourier modes to $\pm f/2$ and $\pm 3f/2$ they showed that the response would be subharmonic if the fluid depth, h, is much greater than the viscous boundary layer $\delta = \sqrt{2\nu/(2\pi f)}$. By further truncating the series of modes to only $\pm f/2$, Müller *et al.* [34] could solve the equations deriving a solution for the Faraday threshold in the limit of large depth and low viscosity.

This approach is followed by Tadrist *et al.* [27]. They first derive an equation for the surface elevation under the assumption that h is much bigger than δ. The result is an integro-differential equation derived under the condition that the amplitude of the surface waves is much smaller than both λ_F and δ. An extra damping term shows up in the integral and is due to bulk waves emitted by the surface waves. Truncating the series of modes to only $\pm f/2$ and assuming a small detuning close to γ_F they proceed to solve analytically for the driven surface waves. Any disturbance then leads to the excitation of long-lived Faraday waves which are detuned by $\pi/4$ close below γ_F.

The impact of the walker is introduced as a series of delta function kicks at times $\tau_n = \tau_i + 2\pi n$, where τ_i denotes the phase of the impact. $n \in \mathbb{Z}$ and normalized time $\tau = (2\pi f/2)t$. The previous bounces of the walker are set to happen at positions $\mathbf{r_n} = -(\tau - \tau_n)\mathbf{v}$, and the drop position $\mathbf{r} = 0$ at time τ. The walker is assumed to move in a straight line with constant velocity and bouncing periodically in sync with

the Faraday waves. Inserting this as an external pressure term, they derive an expression (Eq. (D1) in Ref. [27], Appendix D), for the wave field at position r following the walker,

$$\zeta(\mathbf{r}, \tau) = \sum_{n=-\infty}^{[(\tau-\tau_i)/2\pi]} B_F^+ k_F \sqrt{\frac{\pi}{D_{\mathrm{diff}}(\tau - \tau_n)}} J_0(k_F|\mathbf{r} - \mathbf{r_n}|)$$
$$\times \cos(\tau + \Theta_F^+)\exp\left(-\frac{\tau - \tau_n}{2\pi M_e} - \frac{|\mathbf{r} - \mathbf{r_n}|^2}{4D_{\mathrm{diff}}(\tau - \tau_n)}\right). \tag{3}$$

Here J_0 is the Bessel function of the first kind of order zero.

The upper limit of the sum, denoted $[(\tau - \tau_i)/2\pi]$, is defined as the largest integer smaller than $(\tau - \tau_i)/2\pi$. Θ_F^+ is the phase-shift of the Faraday waves, and as we are mainly interested in the form of the wave field in the limit of $M \gg 1$, we use the simple expression for B_F^+ given in Eq. (2.68b), Ref. [27],

$$B_F^+ = v_F \cos(\tau_i - \pi/4). \tag{4}$$

Here $v_F = 2V_F/(2\pi f)$ with $V_F = \lambda_F \times f/2 \approx 190 \mathrm{\ mm/s}$ being the Faraday wave velocity.

With r measured in mm, the diffusion coefficient $D_{\mathrm{diff}} = 2.20 \mathrm{\ mm}^2$ (see footnote [35]). As normalized time is $(2\pi f t/2)$, the normalized drop velocity is $v = 2V_w/(2\pi f)$. The memory number M_e is given by

$$M_e = \frac{M}{2\pi\gamma_0}\left(1 + \frac{\gamma_0^{1/2}}{2} + \frac{\gamma_0}{4}\right). \tag{5}$$

Here the free damping factor $\gamma_0 = 4\nu k_F^2/(2\pi f)$. With $f = 80 \mathrm{\ Hz}$ and $\nu = 20 \mathrm{\ mPa\ s}$, we have $k_F \approx 1320 \mathrm{\ m}^{-1}$, $\gamma_0 \approx 0.277$, and $M_e \approx 0.76M$. In dimensional form the damping time as given by Tadrist et al. [27] is

$$\tau_M = M_e T_F, \tag{6}$$

where the Faraday period $T_F = 2/f$. To validate the expression for the wave field we have in Fig. 3 compared a simulation on Eq. (3) with a wave field measurement by Rode et al. (see Fig. 4(a) in Ref. [23]). Due to the way the equation for the wave field is constructed, the form of the response is determined by the velocity V_w of the walker and M, while the absolute scale is determined by the choice of τ_i. As seen, especially in the forward direction the fit is excellent with $\tau_i = 0.381$. This value of τ_i agrees well with, e.g., the values used in the simulations by Faria [25]. We note here that the wave height measurements by Rode et al. [23] and also by Damiano et al. [36] show that apart from the central peak, the theoretical condition of the wave height being much smaller than h, λ_F, and δ is fulfilled.

Equation (3) can further be transformed into an integral,

$$\zeta(\mathbf{r}, \tau) = \frac{B_F^+ k_F}{2\sqrt{D_{\mathrm{diff}}}} \cos(\tau + \Theta_F^+)\exp\left(-\frac{vr\cos(\Theta)}{2D_{\mathrm{diff}}}\right)$$
$$\times \int_\pi^\pi \frac{\exp[ik_F r \sin(\Theta - \phi)]}{\sqrt{a - ik_F v \sin(\phi)}}$$
$$\times \exp\left(-\frac{r}{\sqrt{D_{\mathrm{diff}}}}\sqrt{a - ik_F v \sin(\phi)}\right)d\phi, \tag{7}$$
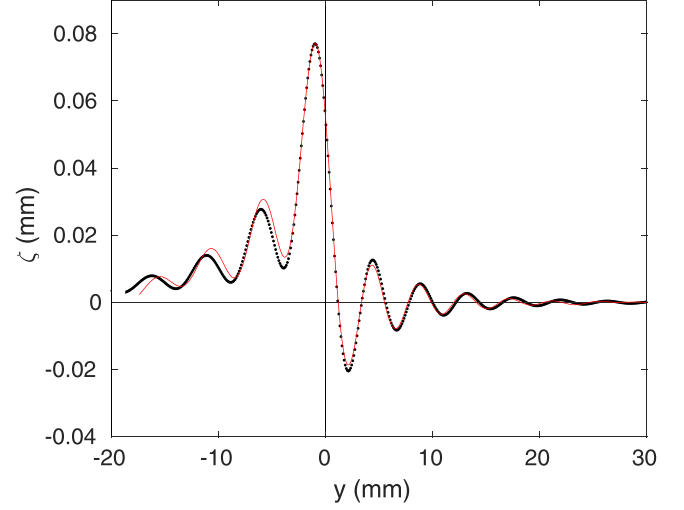

FIG. 3. Wave height measurement (data, courtesy Mads Rode) along the trajectory in the direction of the drop movement. The wave height is measured far from any obstacles and is shown by the continuous (red) curve. The dot-dot (black) curve is a simulation on Eq. (3). Especially in the forward direction the fit is good. Experimental values given are the drop diameter $D = 0.763 \pm 0.003 \mathrm{\ mm}$, and $M = 69 \pm 16$. Since V_w is not stated we have used $V_w = 9.5 \mathrm{\ mm/s}$ as representative in the simulation. $\tau_i = 0.381$, and the summation is taken to $n = 3M$ to ensure convergence.

where

$$a = \frac{1}{2\pi M_e} + \frac{v^2}{4D_{\mathrm{diff}}}. \tag{8}$$

Here Θ denotes the angle in the horizontal plane between the direction of $\mathbf{r}$ and the direction of the velocity of the walker (see Fig. 6 for details). Evaluation of the integral yields the same results as Eq. (3) except that the central peak becomes slightly higher. Our simulations are therefore done on Eq. (3) throughout the paper.

In the limit of small memory factor M and low walker velocity V_w, the square-roots in Eq. (7) can be expanded, and an analytic solution (Eq. (2.59) in Ref. [27]) for the wave field is found,

$$\zeta(\mathbf{r}, t) = \frac{B_F^+ k_F}{\sqrt{v^2 + \frac{2D_{\mathrm{diff}}}{\pi M_e}}} \cos(\tau + \pi/4)$$
$$\times J_0\left(k_F\left|\mathbf{r} + \frac{r}{\sqrt{\left(v^2 + \frac{2D_{\mathrm{diff}}}{\pi M_e}\right)}}\mathbf{v}\right|\right)e^{-r/l(\Theta)}. \tag{9}$$

The condition for the expansion to be valid is $k_F v/a = 4D_{\mathrm{diff}} k_F v/[v^2 + 2D_{\mathrm{diff}}/(\pi M_e)] \approx 2\pi k_F v M_e \ll 1$. However, for this to hold for their standard velocity of $V_w = 11 \mathrm{\ mm/s}$, M needs to be much smaller than 4.8 corresponding to $\gamma/\gamma_F \ll 0.79$, making the approximation of limited value. In fact, comparison of simulations on Eqs. (3) and (9) reveals significant discrepancies.

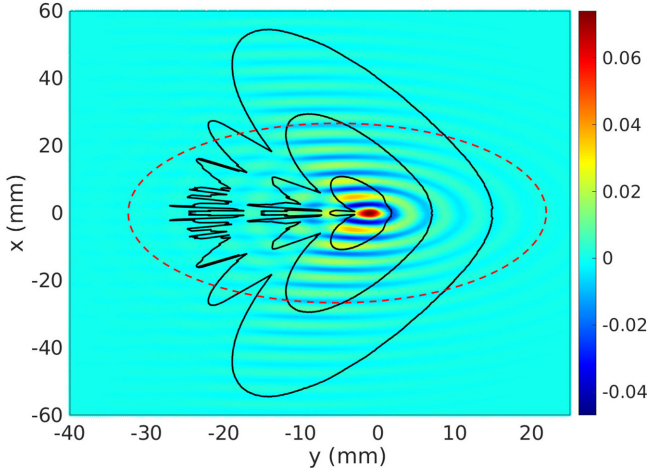Tadrist et al. [27] took Eq. (9) to mean that the accompanying wave field is exponentially damped in space with an

FIG. 4. Simulation on Eq. (3) of the wave field with the drop at the origin and moving right along the y axis. $V_w = 8.2$ mm/s and $M = 67$. The wave height (in mm) is represented by the color-scale to the right. The continuous curves (black) are, counting from the center 30%, 10%, and 3% contour curves. These are seen to even catch some of the destructive interference lines in the wake. $\tau_i = 0.381$. The summation is taken from $n = -3M$ to ensure convergence. The dashed (red) curve is $l(\Theta)$ [Eq. (10)]. This is clearly not following a constant contour.

anisotropic damping length given by

$$l(\Theta) = \frac{2D_{\text{diff}}}{v\cos(\Theta) + \sqrt{\left(v^2 + \frac{2D_{\text{diff}}}{\pi M_e}\right)}}. \qquad (10)$$

At higher values of M and/or faster walkers a simple analytic solution is not possible. However, an upper bound of the wave field is found exhibiting the same exponential decay in space as before. Tadrist *et al.* [27] therefore concluded that the spatial decay also here is governed by $l(\Theta)$.

On the basis of their theoretical investigation Tadrist *et al.* [27] suggested that true interference might be possible in the double-slit experiment under certain conditions and that quantumlike phenomena could occur in the limit of vanishing viscosity (Ref. [27], Appendix F). The posited conditions were that the normalized damping length of the waves, $l(0)_D = l(0)/\sqrt{2}d$, the normalized radius of the container, $R/l(0)$, and the normalized damping time, $\tau_D = M_e T_F V_w/\sqrt{2}d$, all should be much larger than 1. Here the length $\sqrt{2}d$ is chosen as a characteristic path length for moving the drop from one side of the barrier to the other. To fulfill these criteria, γ/γ_F necessarily should be as close to unity as experimentally possible.

Considering Eq. (9) more closely, it is clear that as stated the criteria ignore the decay inherent in the first few periods of the Bessel function J_0. Although we do realize that the criteria are only meant to be a heuristic guide, this simplification unfortunately means that one arrives at overly optimistic criteria. To investigate this aspect, we have made a simulation using Eq. (3) of the wave field with $V_w = 8.2$ mm/s and $M = 67$. The result is presented in Fig. 4.

From the wave field we construct an envelope field $\eta(\mathbf{r})$ defined as the smooth tangent surface that outlines the absolute values of the extremes of the wave field. This is then used to
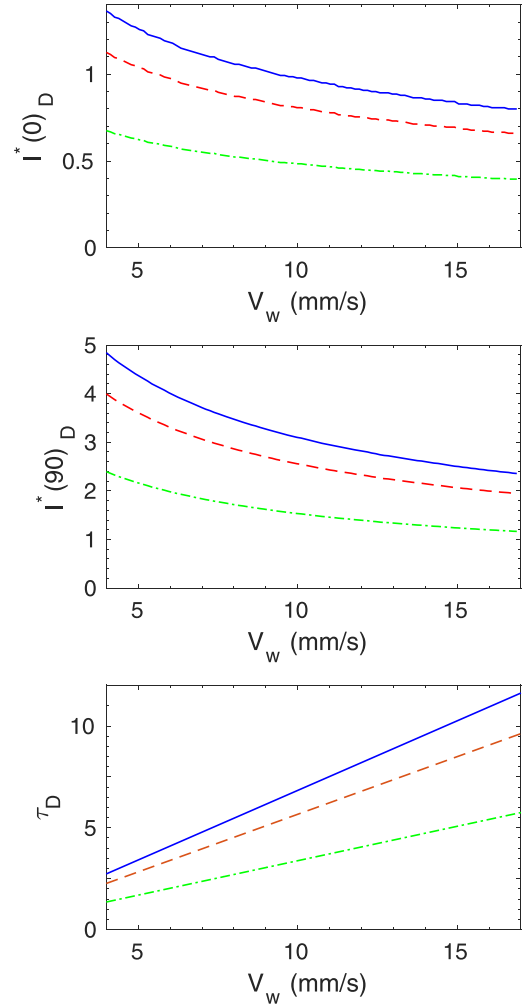

FIG. 5. $l^*(0)_D$, $l^*(90)_D$, and τ_D as functions of V_w for $M = 500$. $(-)$ $L = 5.2$ mm, $(--)$ $L = 7.5$ mm, and $(-\cdot)$ $L = 14.7$ mm.

calculate constant contour curves, along which the envelope field value has fallen to a given percentage of its peak value. Shown are the 30%, 10%, and 3% contours. These even catch some of the destructive interference lines in the wake. Also shown is the ellipsoidal $l(\Theta)$ calculated from Eq. (10). This is clearly not following a constant contour.

Still criteria similar to those proposed are useful in determining an optimum operating point for a double-slit experiment. To obtain a better assessment, though, we replace $l(\Theta)$ in the criteria with $l^*(\Theta)$ equal to the absolute value of the vector $\mathbf{r}$ originating in $(x, y) = (0, 0)$ and having its end point on the 3% contour curve in the direction Θ (Fig. 6).

In Fig. 5 we show the variation of $l^*(0)_D$, $l^*(90)_D$, and τ_D calculated using Eqs. (3) and (6) as function of V_w for three different slit sizes setting $\gamma/\gamma_F = 0.998$. We have included $l^*(90)_D$ since we believe the real quantity of interest is somewhere in-between $l^*(0)_D$ and $l^*(90)_D$. Ignoring for the moment the condition on the size of the container, from this figure it is clear that the slit of highest interest is the $L = 5.2$ mm slit. Also, that the optimum velocity range is around 6–9 mm/s as this is the only region where at least both $l^*(90)_D$, and τ_D are simultaneously $\geqslant 3$. Furthermore,
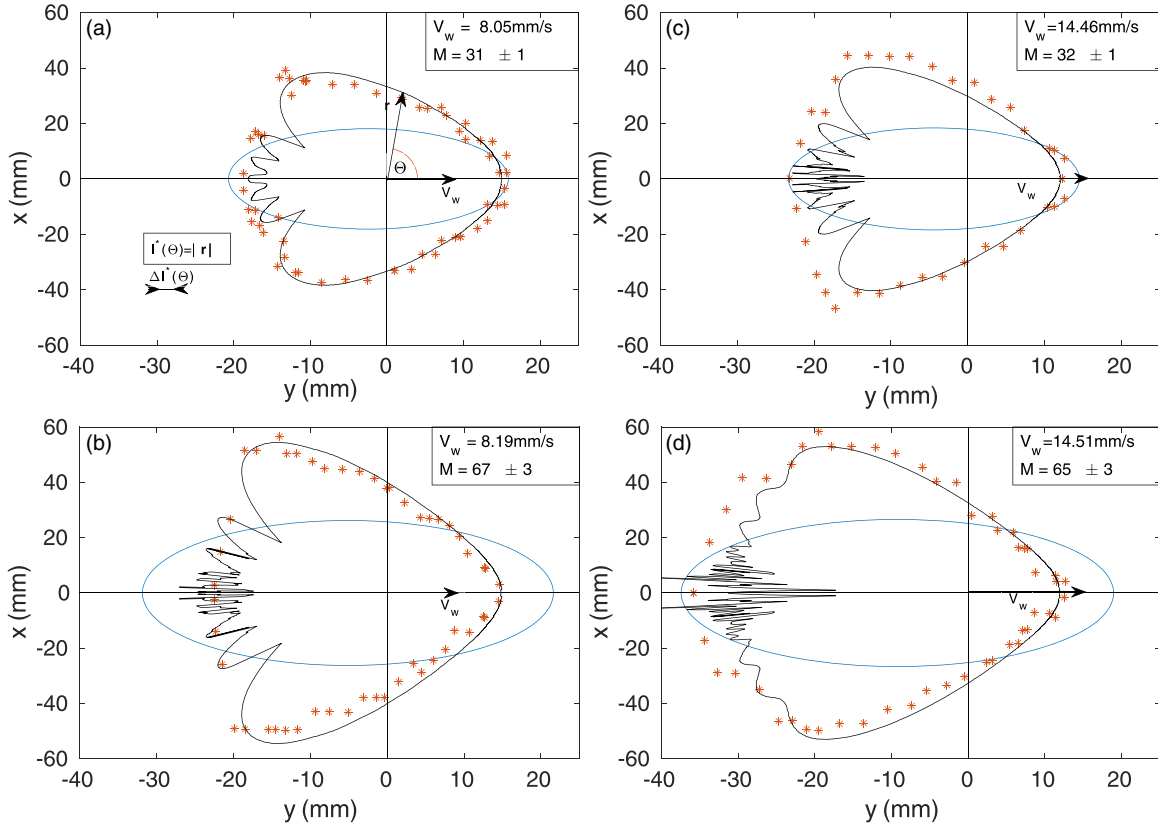
FIG. 6. Measurements of $l^*(\Theta)$. Values of the parameters V_w and M in upper right corner of each field. (a), (b) $D = 0.701 \pm 0.014$ mm. (c), (d) $D = 0.854 \pm 0.012$ mm. The uncertainty on V_w is ± 0.08 mm/s. The direction of the drop is shown by the arrows V_w. The definitions of Θ and $l^*(\Theta)$ are shown in (a) together with the uncertainty in the measurement of $l^*(\Theta)$. Full curves (in black) show the 3% contour lines found using Eq. (3) that as seen give a good fit to the data (∗). Also shown are $l(\Theta)$ (the ellipsoids) calculated from Eq. (10).

that much larger than 1 is impossible to reach experimentally. Still we expect that some traces of nondeterministic behavior could be present if the criteria are at all meaningful.

B. Experimental results

In this section we shall present our results on the spatial and temporal damping of waves associated with the walkers.

1. Spatial damping

Tadrist *et al.* [27] only made a qualitative comparison for $M = 10$ between theory and experiment [their Fig. 3(b)]. The best way to make the measurements would be by using a synthetic schlieren setup. This was done by these authors for their measurement of the decay time. However, a glass bottom and strong lights are at odds with the stringent temperature stability required to reach the high values of M close to the onset of Faraday surface waves that we are aiming at. We therefore resort to a different scheme.

Two strings of small LEDs are placed across the container perpendicular to the direction of the accelerator such that the reflections are seen at distances respectively 63 mm and 92 mm after the end of the accelerator with the latter used to check for possible size effects. Moreover, we have placed a flat dummy in the groove instead of a barrier to create a free path after the accelerator. The size of the deflections by the wave field thus gives a measure of the height of the wave field.

With an exposure time greater than T_F we get a full swing of the deflection from each LED in every frame. To measure the extent of the wave field we follow frame by frame the largest clearly defined fixed size of deflection as it is moved from LED to LED when the walker proceeds along its trajectory. In this way we obtain a contour of fixed amplitude of the wave field around the drop. Ideally we should do this at a wave height of 1/e times the maximum wave height close to the impact position of the drop. Unfortunately we have no way of measuring this peak value, so we end up with an arbitrarily chosen contour. Note, that the window in wave height where this measurement is possible is quite narrow. As shown below the actual measurement turned out to correspond to the 3% level, leading us to choose this as our definition of $l^*(\Theta)$.

The measurement was made at $M \approx 31$ and at $M \approx 66$ for two values of drop sizes with the results displayed in Fig. 6. Also shown for comparison is the 3% contour line calculated from Eq. (3) together with $l(\Theta)$ calculated from Eq. (10).

That the damping is anisotropic is easily discerned, with that of the higher velocity being most prominent. The agreement with the 3% contour line calculated from Eq. (3) is surprisingly good, although the interferences seen in the wake give rise to some deviation. These interferences are also present in the simulations by Tadrist *et al.* [27] and similar to those seen experimentally by Eddi *et al.* [30] in the wave patterns. Note that the form deviates strongly from the ellipsoidal shape of $l(\Theta)$ calculated from Eq. (10).
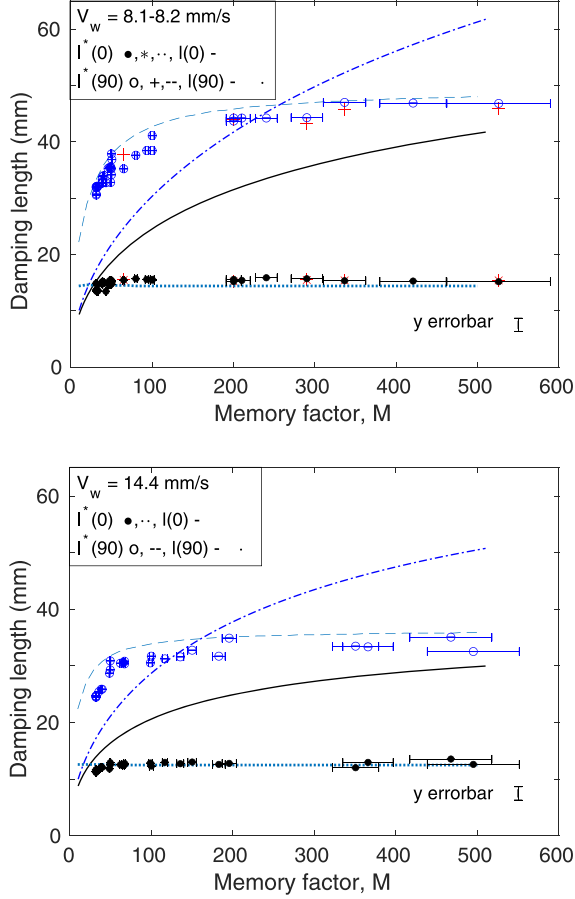
FIG. 7. Measurements of the dependence of $l^*(0)$ and $l^*(90)$ on M (see footnote [37]). (●, black) and (o, blue) from LED line at 63 mm after accelerator, (∗, red) and (+, red) from LED line at 92 mm after accelerator. Upper panel: $D = 0.710 \pm 0.014$ mm, $V_w = 8.1 - 8.2$ mm/s. Lower panel: $D = 0.854 \pm 0.012$ mm, $V_w = 14.4$ mm/s [37]. The simulated 3% contour values from Eq. (3) for $l^*(0)$ (··) and $l^*(90)$ (−−) are plotted too, showing good overall agreement. Also included are $l(0)$ (−) and $l(90)$ (− · −·) calculated from Eq. (10).

For $l^*(0)$ and $l^*(90)$ the investigation has furthermore been extended to cover the interval $30 \leqslant M \leqslant 500$ with the result shown in Fig. 7. We should mention here that for the chosen drop sizes, V_w is nearly independent of M for $M \geqslant 30$.

Some features of the data agree with Eq. (10), for instance $l^*(90)$ is always greater than $l^*(0)$ and the values decrease with increasing velocity. Also in agreement with the prediction by Tadrist *et al.* [27], in both directions we observe the spatial damping length to saturate as also noted by these authors. However, the saturation sets in at much lower values of M than expected from Eq. (10) [see also their Fig. 3(c)]. This result is, again, in remarkable agreement with the result based on the 3% contour line also plotted in the figure (see also footnote [38]).

2. Temporal damping

Besides investigating the spatial decay we have also measured the temporal decay where the prediction of the theory is that $\tau_M = M_e(M)T_F$.
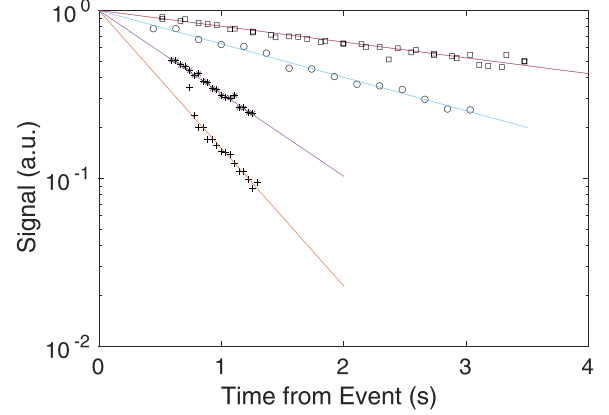

FIG. 8. Measurements of the wave height showing exponential decay with time. Data normalized by extrapolated value at time of absorption of drop. $M = 33 \pm 0.3$ (+), $M = 52 \pm 1$ (∗), $M = 125 \pm 5$ (○), $M = 400 \pm 50$ (□).

Tadrist *et al.* [27] investigated this quantity for $M \leqslant 50$ by dropping glass-beads into an open container. The decay of the waves was again measured by using a synthetic schlieren setup which included the use of high-powered LEDs. As before, this is not feasible close to the onset of Faraday waves both because of heating issues but also due to disturbances from air movement. However, by shooting off large drops and choosing the phase right, these drops will coalesce on impact, very often generating a tiny drop with a diameter smaller than $D = 300$ μm. This will survive for at most a few seconds after which the Faraday waves will start to decay. We can then follow this decay with the method from before. It thus becomes just a question of statistics to obtain good quality data. Some measured decay-curves are displayed in Fig. 8, and as seen we find exponential decay from which we can derive the decay time τ_M as function of M.

In Fig. 9 we show the measured dependence of τ_M on M while also including the data displayed in Tadrist *et al.* [27], their Fig. 7, together with their prediction $\tau_M = M_e T_F$.
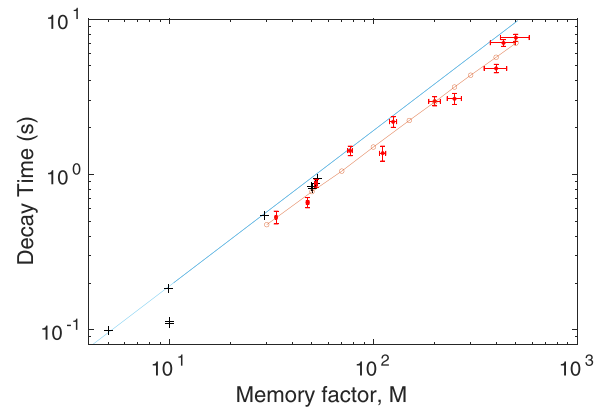

FIG. 9. Measured temporal damping as function of M (●). Also included are the measurements by Tadrist *et al.* [27] (+) (data, courtesy Loïc Tadrist) together with their prediction $\tau_M = M_e(M)T_F$ with $T_F = 25$ ms the Faraday period (−). (○, −−) Simulation based on Eq. (3).
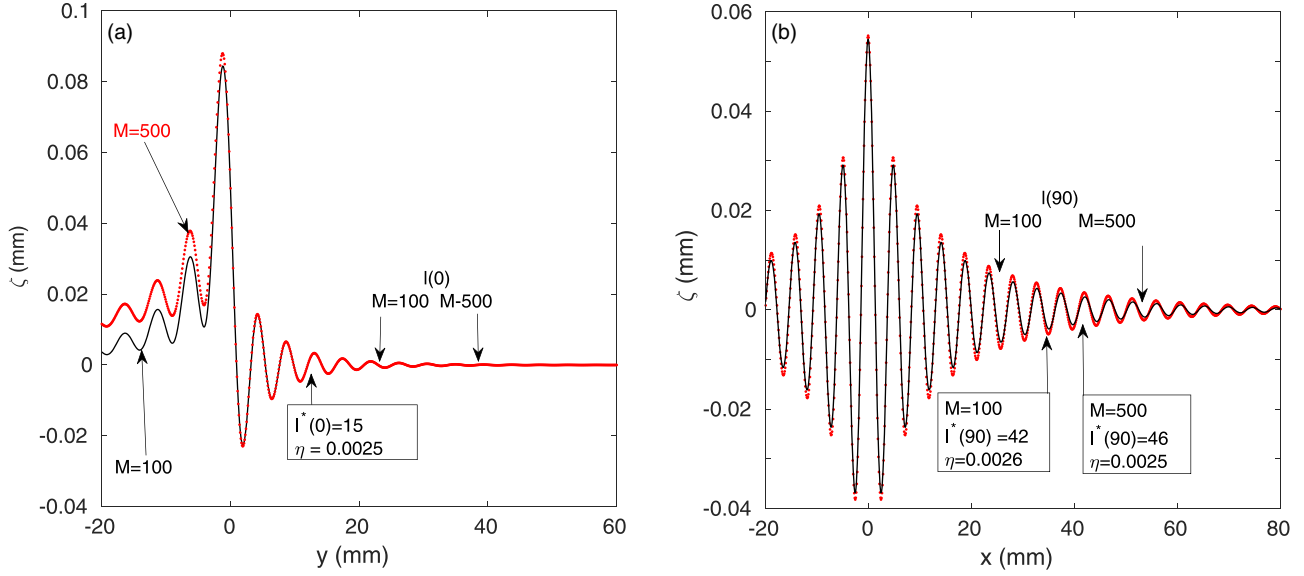
FIG. 10. In panel (a) we show the height of the simulated wave field ζ for $V_w = 8.2$ mm/s with the y-axis following the direction of the trajectory ($\Theta = 0°$). The drop is positioned at $y = 0$. $M = 100$ (–, black) and $M = 500$ (·, red). (b) The same for the wave field height perpendicular to the trajectory ($\Theta = 90°$) for y = 0. The values of the envelope field $\eta(l^*(\Theta))$ corresponding to the measured values of $l^*(\Theta)$ are given in the text boxes with the corresponding arrows pointing to the positions of $l^*(\Theta)$. The positions of $l(\Theta)$ calculated from Eq. (10) are shown with arrows.

Within the experimental accuracy the measured values agree reasonably well with the theoretical prediction. This result was not anticipated. Both Pucci *et al.* [6] and Ellegaard and Levinsen [7] suspected nonlinear effects to be important at high values of M and therefore refrained from using M to characterize the outcome of the slit experiments.

C. Discussion, wave field

In Sec. III B we described the measurements of the spatial and temporal damping that are of importance theoretically. The results on the spatial damping were strongly deviant from the damping term $l(\Theta)$ proposed by Tadrist *et al.* [27]. Most importantly, the spatial damping is seen to saturate much earlier than expected from Eq. (10). As we get the same result from both LED lines where one is rather close to the rim of the container, size effects can be ruled out. A tentative explanation is that the saturation is caused by the drop in every jump trying to overtake the waves in front of it while the waves decay during the jump.

We therefore took a closer look at the theory. Although not all assumptions are strictly met, the comparison shown in Fig. 3 supports the use of Eq. (3). Thus, even though the experiment presumably is done with chaotically bouncing drops, the assumptions on the wave height, the use of δ functions, and of periodically bouncing drops, are all validated. The real problem with the interpretation giving rise to the criteria set out in Ref. [27], however, becomes clear with inspection of Fig. 10. As seen in Fig. 10(a), in the forward direction it is impossible to distinguish between the results for $\zeta(y)$ for $M = 100$ or 500 in agreement with the saturation found in our experiments. For $\Theta = 90°$, Fig. 10(b), we find the same situation to a very high degree. Only in the wake for $\Theta = 180°$, is found a notable difference. For higher values of V_w

(e.g., 14.4 mm/s) even the small difference seen in Fig. 10(b) has disappeared. This shows that the early saturation found experimentally is real with a surprisingly good fit to the full theory.

The experimental values are seen from Figs. 10(a) and 10(b) to correspond to where the envelope field η has fallen to 3% of its maximum value in near perfect agreement with the fit based on the 3% contour line to our measurements displayed in Figs. 6 and 7, although the complicated interference pattern in the wake is giving rise to some deviation. This means that we can actually use results based on simulations on Eq. (3) in the criteria instead.

Turning now to considering the temporal decay we notice from Fig. 9 that generally the measured data points lie below the theoretical value. This discrepancy is caused by $M_e T_F$ being the decay time for a spatially uniform field, while our measurements as well as the measurements of Tadrist *et al.* [27] are done on a localized field. The decay of the field at any given point in space is therefore partly due to dissipation and partly to redistribution of energy from high amplitude regions in the field into low amplitude regions as the field over time becomes more uniform.

This is confirmed by simulations on the full equation. Here we follow the decay of the absolute value of the wave field, Eq. (3), period by period, by letting time τ proceed as $\tau_i + 2\pi(l - 1)$, where $l \in \mathbb{N}$, without new bounces. In Eq. (3) that corresponds to letting τ grow while keeping the last impact at $\tau_i - 2\pi$ thus replacing the upper limit in the sum with just $n = -1$. To keep at a fixed point in space, $\boldsymbol{r_n}$ is replaced with $\boldsymbol{r_n} = -(\tau_i - \tau_n)\,\boldsymbol{v}$. As the energy of a wave field is proportional to the amplitude squared [39], we can follow the energy flow by calculating δE as

$$\delta E(\mathbf{r}, \tau) = \zeta(\mathbf{r}, \tau + 2\pi)^2 - [\zeta(\mathbf{r}, \tau)\exp(-1/M_e)]^2. \quad (11)$$
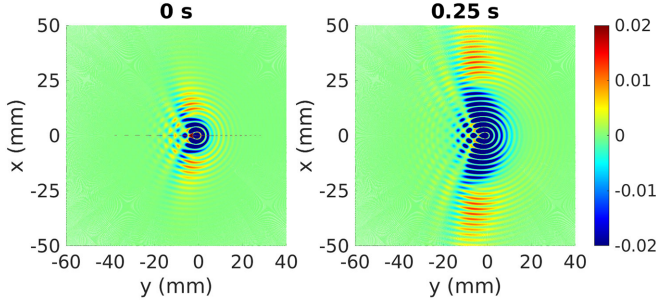
FIG. 11. Simulation of the change in energy distribution $\delta E / \max(\delta E)$ during the decay of the wave field by comparing the actual energy decay with that of a uniform decay after time t. $M = 67$ and $V_w = 8.2$ mm/s with the y-axis following the direction of the trajectory ($\Theta = 0°$). Time proceeds from $t = (\tau - \tau_i)/(\pi f) = 0$ without any new impacts (see text for more details). The decay is followed for one period after the elapsed time noted above the fields. Note the narrowed color range accentuating the outward flow of energy.
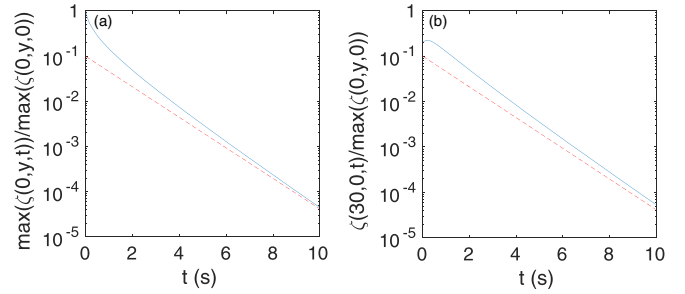

FIG. 12. (a) The decay of the amplitude of the central peak with time showing the initial fast loss of energy followed by a slow approach to the theoretical decay (red $--$) of a uniform field determined by $M_e T_F = 1.27$ s. (b) The same for the wave field amplitude perpendicular to the trajectory ($\Theta = 90°$) $(x,y) = (30,0)$. Here we see the effect of the bleeding of the energy from the higher amplitude in the wake in the initial increase of the amplitude. It takes a surprisingly long time before we approach the decay of a homogeneous field. All fields are normalized by the value at the central peak at time $t = 0$.

Here the first term represents the simulated decay of the amplitude over one period starting at time τ, and the second term the decay over the same period as it would be if the field were to decay uniformly. The choice of τ ensures that $\zeta(\mathbf{r}, \tau)^2$ represents the local amplitude squared. Simulations of δE starting at $t = 0$ and at $t = 0.25$ s are shown in Fig. 11 for parameters $M = 67$ and $V_w = 8.2$ mm/s with δE normalized by $\max(\delta E)$. Notice that the color scale only covers a small part of the total range of energy change to emphasize the energy flow. As seen, there is a faster loss of energy from the high energy regions in the center and in the wake and a corresponding slower loss of energy from the adjacent lower energy regions, thus illustrating the energy flow. Here the blue regions are losing energy while the yellow/red regions are gaining energy compared to uniform decay.

Considering a point away from the center, simulations show that the wave height may actually start to grow due to the redistribution of field energy before the viscous dissipation starts to dominate. The decay of the central peak and the wave field at $(x,y) = (30,0)$ is shown in Fig. 12. It is clear from Figs. 11 and 12 that the inhomogeneity of the field is felt for a surprisingly long time resulting in a lowered value for the measured time constant compared to the theoretical value. As the measurements of the temporal decay is done around $\zeta/\max(\zeta) \approx 0.01$ we have read the slope here from Fig. 12. The result shown as the broken line in Fig. 9 is in fine agreement with the experimental result taking the different drop sizes into account.

IV. MEASUREMENTS WITH SLIT STRUCTURES

Although the reformulated criteria probably can not be fulfilled with the present setup, we should at least be able to get close enough to observe traces of true interference. As shown in Fig. 5, a straightforward use of the conditions for fixed value of M somewhat favors a medium range drop velocity, with the spatial criteria favoring low velocity while the temporal criterion favors high velocity. Furthermore, as pointed out by Pucci *et al.* [6], the bouncing of the low velocity

walkers is chaotic with these authors claiming to have discovered a small region of chaotic response for even a single-slit structure.

We have therefore extended our earlier investigation into the interaction of drops with slit structures [7] both toward lower and higher velocities, thus also probing the boundaries for passage. As already noted in Refs. [6,7], the width, L, of the slits sets a limit to the lowest velocity possible for transit. However, we also found that a similar limitation existed at high velocities even before reaching the high velocity limit for walkers. Measurements regarding this are presented in the figures and captions of Appendix A.

Before going into details about the experimental results, we want to divide the trajectories passing the slit structure into two main categories. We denote trajectories in the first category as regular. Trajectories in this group are smooth and have no kinks or cusps [40] created by stop and go motion, and belong to drops that do not suffer a complete loss of velocity at any time and after passage of a slit leave the immediate neighborhood on a linear trajectory. All other trajectories belong to the irregular category having kinks or cusps where the velocity vector changes direction abruptly, although as we shall show later, they mainly fall into two distinctive groups. Examples of irregular trajectories with kinks are shown in Fig. 16 where all the trajectories bending backwards toward the barrier stop, before they make the backward bend. A few of these are shown in the inset.

A. Low velocity regime

The low velocity regime has been investigated for three different single-slits with L equal to 5.2, 7.5, and 14.7 mm, respectively, and $b = 5$ mm. This was done for a wide range of fluid heights h_1. In the whole regime the response is non-chaotic, as also found in the part of the regime previously investigated. However, a finite low velocity limit, V_{low}, was found that depended on slit size, fluid height, and γ/γ_F. A typical example of trajectories obtained just at the lower limit for transit is shown in Fig. 13. This example extends the result
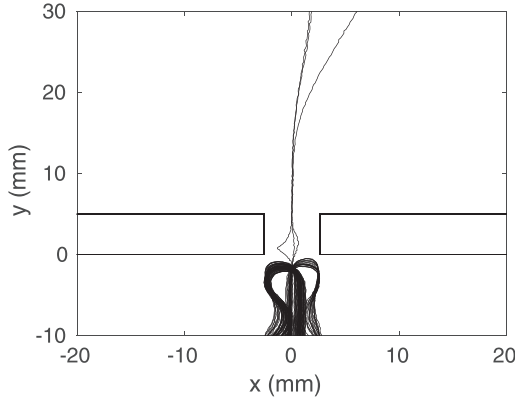
FIG. 13. Typical example of trajectories obtained for a drop velocity just at the lower limit for passage through a $b = 5$ mm and $L = 5.2$ mm single-slit. Trajectories of a total of 20 drops are shown. Of these, two pass in the center following regular trajectories. One drop makes a complete stop in the slit before moving on and turning to the right. $V_{imp} = 7.87 \pm 0.05$ mm/s, $D = 0.713 \pm 0.020$ mm. $\gamma/\gamma_F = 0.998$. $h_1 = 0.550 \pm 0.040$ mm.

for $L = 5.2$ mm shown in Figs. 5 and 6 in Ref. [7] toward the low velocity limit.

A common feature is that the window of impact parameters leading to passage shrinks towards the central part of the slit when V_w is lowered towards V_{low}. Below this, all trajectories are turned away before entering the slit. Both features are present in the figure. The limiting velocity becomes smaller with both increasing fluid height and increasing slit size, showing that the effective slit size becomes larger when the fluid height over the barrier is increased. This trend is clearly seen in Fig. 14 that presents an overview of our results. Moreover, the limit is at its lowest at $\gamma \approx \gamma_F$. Not surprisingly, the above results are also valid in the double-slit cases investigated with $L \leqslant 14.7$ mm (see also Ref. [6]).

B. High velocity regime

Previous investigations have mainly been concerned with walkers inside the regime of the (γ, Ω) phase space where
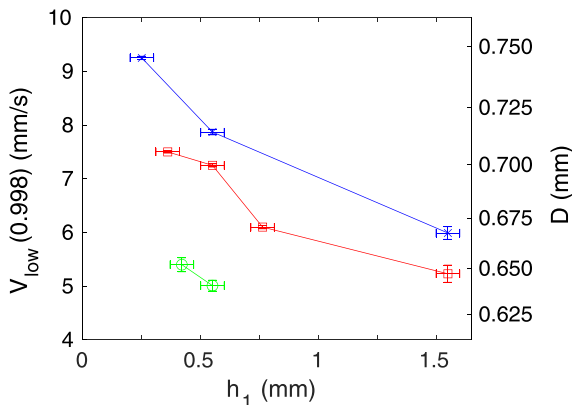

FIG. 14. Low velocity limit $V_{low}(\gamma/\gamma_F)$ with $\gamma/\gamma_F = 0.998$ versus fluid height h_1 over barrier. $L = 5.2$ mm slit (x), $L = 7.5$ mm slit ($\square$), $L = 14.7$ mm slit ($\circ$). The drop size corresponding to $V_{low}(0.998)$ is shown to the right of the figure.

walkers are bouncing chaotically (see Fig. 1). With γ/γ_F equal to 0.998, this corresponds to velocities, V_w, smaller than approximately 11–12 mm/s. Since short transit times are favored at fixed M by the reformulated criteria, we have now investigated the part of the phase space above toward the upper limit of Ω for walkers using the same slit structures as before. This limit also corresponds to the highest possible velocity of around 16.7 mm/s. As before, the outcome is found to be nonchaotic in the whole regime. The expectation here was that for all sizes of the slits, transit would happen all the way up to the upper limit for walkers. The situation, however, was seen to be quite different as instead a lower slit-dependent limit for transit was found.

A common feature here is that the limits are insensitive to acceleration close to γ_F. This, however, is not surprising as the velocity of large drops is nearly constant in this regime of acceleration. That the effective slit size depends on the fluid height does give rise to the limits being slightly dependent on this quantity. When the velocity is raised towards the limit, in all cases we find a transition region. Below this, the trajectories outside the window for regular transit are all turned back before entrance of the slits with the occasional exception of a few back-tracking trajectories as also seen at lower velocities. In the transition region the impact window for passage along regular trajectories is gradually squeezed with the rest of the original window now being occupied by drops following irregular trajectories that stop abruptly just after leaving the slit structure. Even more surprising is the development of a central zone, with or without satellites, where regular trajectories are forbidden, and only the same type of irregular trajectories are found. Finally, at the end of the transition region, these irregular trajectories are the only ones present, even though the window of passage is nearly the same size as before we entered this region.

In Appendix A we show some typical examples of the behavior in the transition region, while our results are summarized in the (V_w, L) phase space displayed in Fig. 15. The velocity $V_w(\gamma/\gamma_F)$, where $\gamma/\gamma_F \approx 0.998$, is here changed by choosing different drop sizes with the connection between $V_w(0.998)$ and Ω (thus D) shown in the figure. In the figure the horizontal light blue shaded area shows the approximate upper boundary for walkers above which only stationary bouncers exist. The vertical, dashed, lines denote the slit sizes L, while the values of x_{imp} leading to regular trajectories for the slit in question are shown with small squares. The spaces in between marked with thin line segments (red) are only occupied by irregular trajectories, the narrow $L = 5.2$ mm slit being distinguished by having satellites to the central zone. The transition always takes place over a quite narrow range of velocity inside the dark gray shaded area which stretches across the figure. For the $L = 14.7$ mm slit the velocity comes close to the highest possible velocity for a walker but still with a notable gap up to this. In the white region above the transition region no regular trajectories are found at all, and drops stop completely after passing. This general behavior has been observed in an interval of fluid height over the barrier from 0.330 mm until 0.650 mm. In the light gray region all passing trajectories are regular except for the occasional back-bending trajectories.

While we only show results for the $b = 5$ mm, $L = 5.2$, 7.5, and 14.7 mm single-slits, we do find similar results for
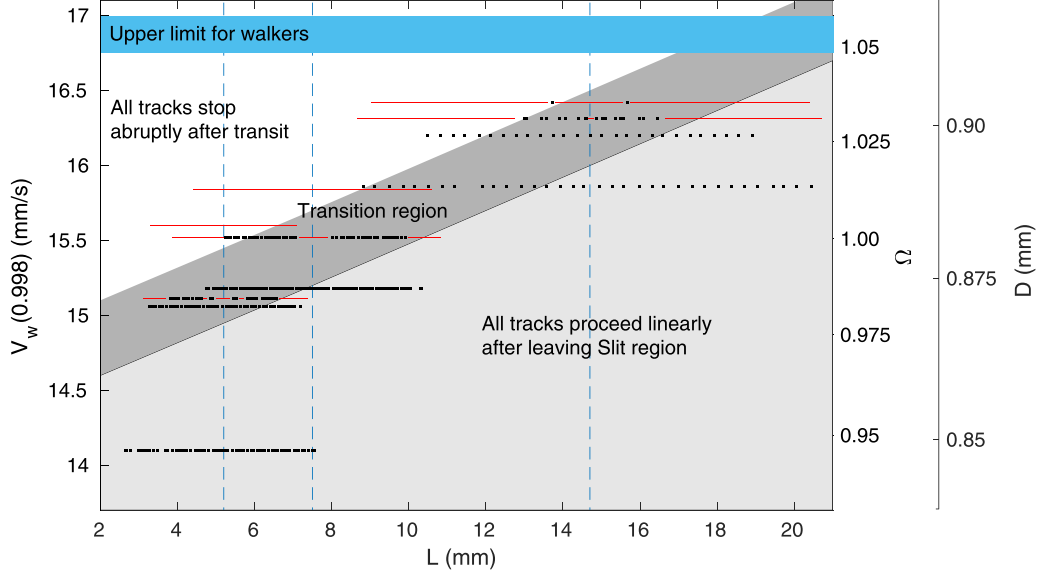
FIG. 15. (V_w, L) phase space with the transition zone approximately covered by the dark gray shaded area. The trajectories in the light gray area belong to either regular or the occasional backtracking, with all trajectories that pass through the slit going on. In the white region above the transition zone, all drops stop completely after passage. The velocity $V_w(\gamma/\gamma_F)$, at $\gamma/\gamma_F = 0.998$, is changed by choosing different drop sizes, and the correspondence between V_w, Ω, and D is shown by adding the right y-axes. The horizontal light blue shaded area shows the approximate upper boundary for walkers. Above only stationary bouncers exist. The vertical, dashed, lines denote the slit sizes L. The impact range x_{imp} for the different slits are centered around the vertical lines denoting the slit sizes—and shown on the same scale. The values of x_{imp} leading to regular trajectories are shown with small squares, while the thin (red) horizontal lines show the parts of the impact ranges x_{imp} occupied by trajectories that stop abruptly after passage.

all other single slits regardless of the value of b as well as for all double-slits. In the case of a regular barrier high velocity walkers will also come to a complete stop. For low fluid heights this happens when the walker approach the barrier. This may be considered as the limit of $L \to 0$ case. At sufficiently high fluid heights it will happen after passage of the barrier.

C. Implications for the double slit experiment

We now return to whether the double-slit experiment may result in true interference and/or chaotic behavior keeping in mind the limitations mentioned above. From Fig. 5 it is clear that for observation of true interference, the $L = 5.2$ mm slit is of highest interest. Furthermore, the velocity range should be around 6–9 mm/s for $l^*(\Theta)_D$, τ_D, and $R/l^*(0)$ all to be simultaneously at least $\geqslant 3$. Finally, γ/γ_F should be as close to unity as experimentally possible.

This velocity and γ regime we have already covered extensively using $b = 5$ mm barriers with $L = 5$, 7.3, and 7.5 mm wide double-slit structures and $L = 14.7$ mm single-slits [7]. We have now extended the investigation to cover the whole possible velocity range for these slits and find that the connection between the angular deflection angle α and the impact parameter x_{imp} is always without any sign of true interference and also nonchaotic.

A critical feature of the temporal criterion is, that it is tacitly assumed that the breadth b of the slit is negligible. This can be seen from the use of the free space drop velocity, V_w, in calculating τ_D. However, in reality the velocity of the walker decreases appreciably during passage as, e.g., seen in the left

inset of Fig. 16(a) for a $b = 2$ mm barrier. Simultaneously the trajectory is often very far from straight as most clearly seen in the figures of Appendix A. These effects are also seen in Fig. 5, of Ref. [23], where the wave field in the unused slit furthermore can be seen to deteriorate visibly during the passage of the drop through the other slit.

For $b = 4$–6 mm, a realistic value of T_{ch} can be substantially larger than l_{ch}/V_w. Including this in the estimate of τ_D can thus lower this quantity a great deal. As this might well be the reason why no trace of true interference or chaotic behavior has been encountered so far, we have made a series of measurements on $b = 2$ mm ($L = 5.2$ mm), and $b = 0.5$ mm ($L = 5.2$ and 7.3 mm) slits covering the range of 6 to 17 mm/s with γ/γ_F between ≈ 0.97 and 1.

1. $b = 2$ mm barrier with double-slit

The measurements with a $b = 2$ mm double-slit barrier show a similar picture to those described earlier for the $b = 5$ mm barrier with trajectories fanning out after passage. The response shows no sign of true interference, although we still see the distortion stemming from the waves scattered from the backside of the barrier. Furthermore, the response is always nonchaotic.

Up to a limiting velocity as described above we observe smooth regular trajectories surrounded by trajectories that turn back before entering the slit together with the occasional back-tracking trajectories also seen for the $b = 5$ mm barrier. An example from below the limiting velocity is displayed in Fig. 16. Of 47 trajectories passing, 30 trajectories are smoothly regular, always having a nonzero velocity. A single
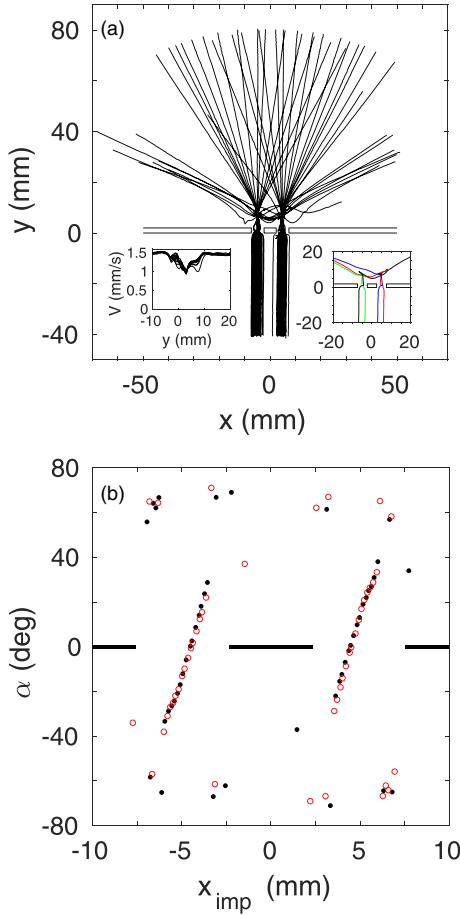
FIG. 16. Double-slit experiment with $b = 2\,\mathrm{mm}$ barrier, $L = 5.2\,\mathrm{mm}$, and $d = 9.9\,\mathrm{mm}$ (47 trajectories). $\gamma/\gamma_F = 0.998$, and $h_1 = 0.620 \pm 0.040\,\mathrm{mm}$. Impact velocity of $14.51 \pm 0.02\,\mathrm{mm/s}$ and $D = 0.863 \pm 0.020\,\mathrm{mm}$. (a) All passing trajectories. The right inset shows a few of the irregular trajectories while the left shows the velocity change during passage. (b) The associated distribution of angular deflection, α ($\bullet$), including also the far field response of any irregular trajectories, as function of the impact parameter x_{imp}. The nonchaotic nature is high-lighted by also plotting a point symmetric copy of the response ($\circ$). The black line segments at $\alpha = 0$ symbolize the barrier with slit openings.

smooth trajectory, coming from the left slit and passing all the way across the right slit, slightly backtracks before curving away and proceeding in a straight fashion. Such trajectories were also observed for the $L = 14.7\,\mathrm{mm}$ double-slit by Pucci *et al.* [6] both in experiments and simulations [their Figs. 7(a) and 7(d)]. The remaining irregular trajectories all belong to the class where the drops stop, turn back towards the barrier before turning again and proceeding in a regular fashion. But even these trajectories are reproducible with some shown in the inset to the right of Fig. 16(a).

As expected the average of the time T_s spent in the slit, approximately 0.15 s, is not as detrimental as in the case of the $b = 5\,\mathrm{mm}$ barrier, where $\langle T_s \rangle$ for the same velocity is approximately 0.55 s. These numbers should be compared to the characteristic time T_{ch} of 0.96 s.

For higher velocities we find a transition region as described above with forbidden zones occupied by irregular

trajectories where the drops come to a complete stop after passage. But the message is clear. In the whole velocity interval, where walkers can pass, the relation between α and x_{imp} is nonchaotic for all values of γ. Also, there is no sign of true interference with the angular distribution just being a slightly skewed version of that for the corresponding single-slit.

2. $b = 0.5\,\mathrm{mm}$ *barrier with double-slit*

Experiments with the $b = 0.5\,\mathrm{mm}$ double-slit barriers were done at fluid heights h_1 from 0.410 to 0.960 mm. Generally the results are remarkably similar to those seen for the $b = 2$ and 5 mm barriers. The drops passing through the slits exhibit the same symmetry-broken angular response as is seen for those slits, with the interaction of the wake with the other slit still being the deciding factor in the outcome. This is illustrated by the measurements displayed in Fig. 17 ($L = 5.2\,\mathrm{mm}$) and Fig. 18 ($L = 7.3\,\mathrm{mm}$). In the figures we only show regular trajectories, having excluded trajectories belonging to drops that hit the central block or the outer edges of the slits and are turned back.

In the case of the $L = 5.2\,\mathrm{mm}$ double-slit most trajectories never cross from one side to the other, i.e. trajectories originating on the left side of a slit have negative deflection angles while trajectories originating on the right side of a slit have positive deflection angles. Only at the outskirts, we observe trajectories that suddenly start crossing. Examples of the two different cases are shown in the inset of Fig. 17(a) with a magnified view. These crossing trajectories give rise to the vaselike structure seen in the figure, and the rapid shift of sign in Fig. 17(b).

In the case of the $L = 7.3\,\mathrm{mm}$ double-slit the pattern at $V_w \approx 9\,\mathrm{mm/s}$ is slightly more complicated. In the interior trajectories coming from the left side of a slit have a small overlap with trajectories originating from the right side hence resulting in two crossings. Thus, the outcome for the deflection angles is as for the $L = 5.2\,\mathrm{mm}$ double-slit. At the outskirts, however, the structure is more complicated with trajectories having nearly identical input values of x_{imp} ending up nearly 100° from each other although still reproducible. Examples of the different outcomes are displayed in the insert of Fig. 18(a) and are reflected in the more complicated structure of Fig. 18(b).

An interesting new feature is found when fluid heights are increased to above $\approx 0.800\,\mathrm{mm}$. Here high velocity drops pass over the barrier outside the region of the slits as described in tunneling papers, e.g., Ref. [14]. Far from the slits these trajectories are not influenced, but close by they are strongly affected by the interaction of the wake with the slits. Nevertheless, the drops passing through the slits seem to be quite unaffected with the interaction of the wake with the other slit still being the deciding factor in the outcome. An example for a single-slit is shown in Appendix B, Fig. 24.

3. *Time spent in the slit*

In Fig. 19, the delay caused by the velocity loss and the prolonged route taken by most drops during passage of the $L = 5.2\,\mathrm{mm}$ double-slits is illustrated by typical examples for barriers with $b = 5$, 2, and 0.5 mm.
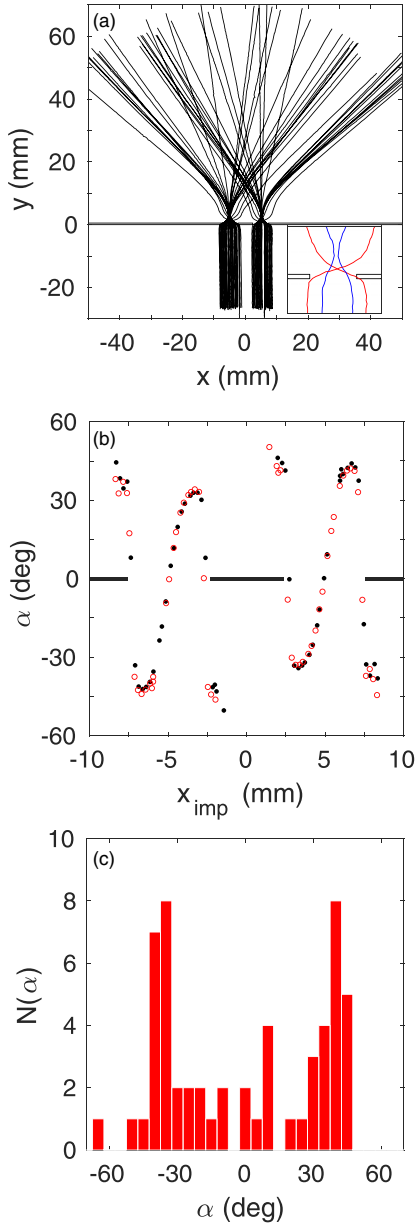
FIG. 17. Double-slit experiment with a $b = 0.5$ mm barrier, $L = 5.2$ mm, and $d = 9.9$ mm (55 trajectories). Impact velocity $V_w = 12.63 \pm 0.08$ mm/s and drop size $D = 0.849 \pm 0.016$ mm. $\gamma/\gamma_F = 0.998$, and $h_1 = 0.670 \pm 0.040$ mm. (a) All trajectories that pass through the slits with the inset displaying a 10 by 10 mm section around the slit to the right showing the different types of trajectories found. (b) The associated distribution of angular deflection (●) as function of the impact parameter x_{imp}. To illustrate the reproducibility we have also shown the point-symmetric response (○). The line segments at $\alpha = 0$ symbolize the barrier with slit openings. (c) Histogram of angular distribution.
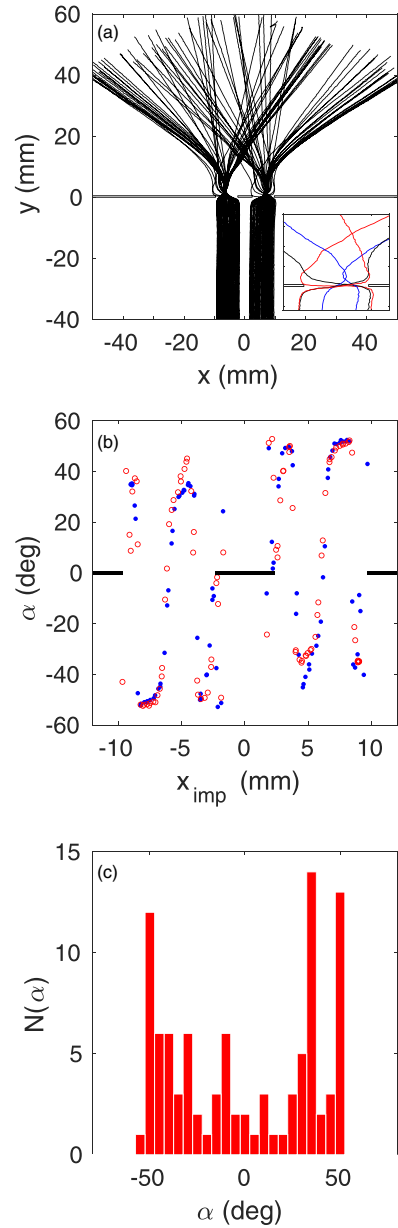

FIG. 18. Double-slit experiment with a $b = 0.5$ mm barrier, $L = 7.3$ mm, and $d = 12$ mm (96 trajectories). Impact velocity $V_w = 9.03 \pm 0.08$ mm/s and drop size $D = 0.724 \pm 0.010$ mm. $\gamma/\gamma_F = 0.998$, and $h_1 = 0.740 \pm 0.040$ mm. (a) All trajectories that pass through the slits with the inset displaying a 12 by 24 mm section around the slit to the right showing the different types of trajectories found. (b) The associated distribution of angular deflection (●) as function of the impact parameter x_{imp}. To illustrate the reproducibility we have also shown the point-symmetric response (○). The line segments at $\alpha = 0$ symbolize the barrier with slit openings. (c) Histogram of angular distribution.

As we have to open the container to change the slit structure, drop sizes will be slightly different. The response of the deflection angle α versus the impact parameter x_{imp} for the three barriers are displayed in Figs. 19(a)–19(c). The corresponding characteristic times T_{ch} are 1.27, 1.44, and 1.39 s, respectively. In Fig. 19(d) we compare the measured times

spent in the slit T_s, normalized with the characteristic time T_{ch}, versus x_{imp}.

In all cases we find a simple U-shaped response having a large overall change across x_{imp}. Even though the fluid height is seen to have a great influence on the range in x_{imp} that is occupied, the minimum time spent scales nicely with b, with the delay being significant for $b = 5$ mm but negligible for
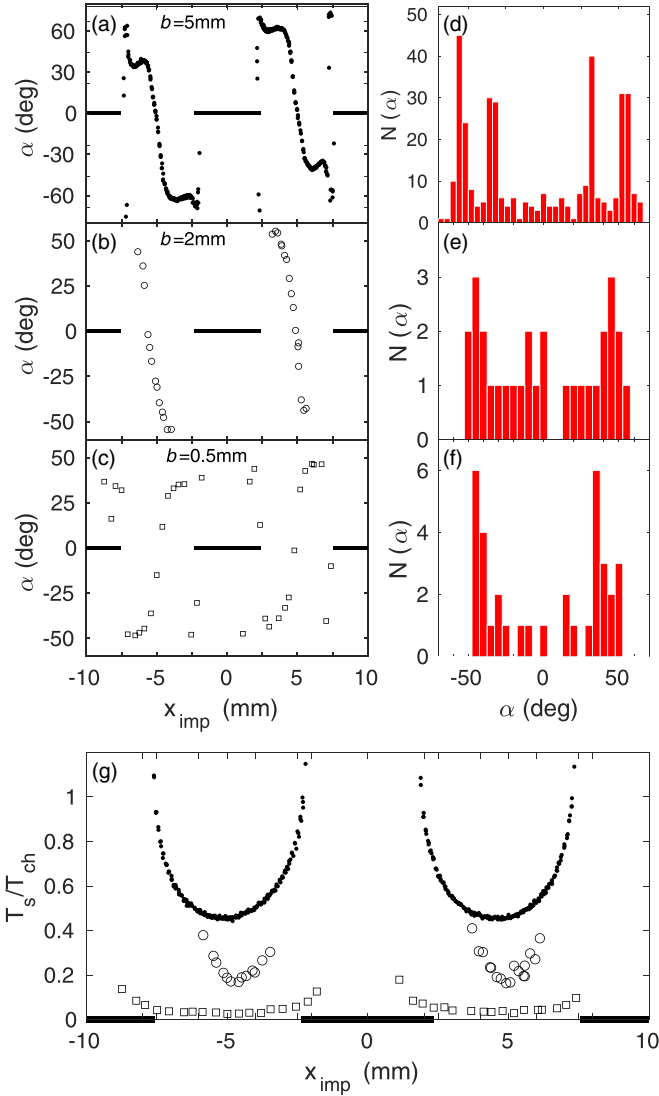
FIG. 19. Deflection angle α versus x_{imp} for a double-slit experiment with $L = 5.2$ mm and $d = 9.9$ mm. (a) $b = 5$ mm, 362 trajectories, $D = 0.820 \pm 0.015$ mm, $V_w = 10.91 \pm 0.04$ mm/s, $h_1 = 0.710 \pm 0.040$ mm, (b) $b = 2$ mm, 30 trajectories, $D = 0.756 \pm 0.015$ mm, $V_w = 9.71 \pm 0.04$ mm/s, $h_1 = 0.540 \pm 0.040$ mm, (c) $b = 0.5$ mm, 35 trajectories, $D = 0.821 \pm 0.016$ mm, $V_w = 10.01 \pm 0.04$ mm/s, $h_1 = 0.710 \pm 0.040$ mm. (d)–(f) Corresponding histograms of angular distribution. (g) Measured time spent inside the slit T_s normalized with the characteristic time T_{ch} versus x_{imp} for the above. $b = 5$ mm (●), $b = 2$ mm (○), and $b = 0.5$ mm (□). $\gamma / \gamma_F = 0.998$. The line segments at $\alpha = 0$ (a)–(f) and at $T_s / T_{\mathrm{ch}} = 0$ (g) symbolize the barrier with slit openings.

$b = 0.5$ mm. This comparison shows that b plays an important role in the interpretation of the experiment.

A similar comparison is carried out in Fig. 20 for $L = 7.3$ mm double-slits with $b = 5$ mm and $b = 0.5$ mm. The characteristic time T_{ch} is here 1.80 s. The angular response for the $L = 7.3$ mm double-slit is rather complicated. But interestingly, the variation of T_s across the slit openings still has a quite simple form with the smallest delay found in the central regions of the slits. Again the delay is rather significant for the $b = 5$ mm barrier and negligible for the $b = 0.5$ mm barrier.
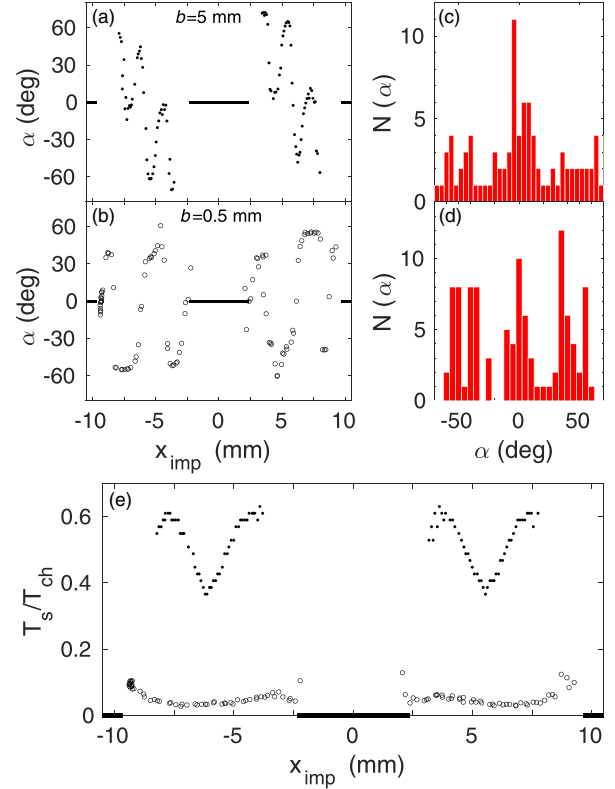

FIG. 20. Deflection angle α versus x_{imp} for a double-slit with $L = 7.3$ mm, $d = 12$ mm. (a) $b = 5$ mm, 94 trajectories, $V_w = 9.30 \pm 0.04$ mm/s, and $D = 0.730 \pm 0.015$ mm. $h_1 = 0.780 \pm 0.040$ mm. (b) $b = 0.5$ mm, 104 trajectories, $V_w = 9.27 \pm 0.07$ mm/s, and $D = 0.750 \pm 0.015$ mm. $h_1 = 0.540 \pm 0.040$ mm. $\gamma / \gamma_F = 0.998$ for both. (c), (d) Corresponding histograms of angular distribution. (e) Measured time spent inside the slit T_s normalized with the characteristic time T_{ch} versus x_{imp} for the above. $b = 5$ mm (●), and $b = 0.5$ mm (○). The line segments at $\alpha = 0$ (a)–(d) and at $T_s / T_{\mathrm{ch}} = 0$ (e) symbolize the barrier with slit openings.

4. Behavior in and close to the slit

Here we shall only deal with the behavior close to γ_F, i.e., at $\gamma / \gamma_F \approx 0.998$.

Although the fanning out of trajectories after passage looks deceptively alike for all $L = 5.2$ mm barriers, the detailed structure is varying. The dominant feature for the $b = 5$ mm barrier is that trajectories starting from one side of the slit end up at the other side thus crossing the center-line an odd number of times; see, e.g., Fig. 21(e). For the $b = 2$ mm barrier this is also the case for low velocity drops. However, for high velocity drops the dominant feature is an even (0 or 2) number of crossings (see Fig. 16). For the $b = 0.5$ mm barrier an even number of crossings dominate at all drop velocities, although 1 crossing is seen for high numerical values of x_{imp} (Fig. 17). This is the cause of the shift in symmetry seen in Fig. 19. Here, compared to the $b = 5$ mm (a) and $b = 2$ mm (b) barriers, that have an odd number of crossings, the $b = 0.5$ mm barrier (c) has zero crossings, indicating that the time spent in the slit is an important factor in the resulting symmetry.

For $b = 5$ mm, at $L = 7.5$ (and 7.3 mm) we find that the number of crossings can be at least 1, 2, or 3 (see, e.g., Fig. 22

TABLE II. Overview of experimental conditions used in previous double-slit experiments compared with some from the present investigation. V_w is the droplet velocity, d the distance between slit centers, and R is the radius of the deep section of the container. The normalized damping time $M_e T_F V_w / \sqrt{2}d$, and the normalized damping length $l/\sqrt{2}d$ are calculated using the theory of Tadrist *et al.* [27]. Compared to the corresponding tables in Refs. [7,27], the entry for Couder and Fort has been corrected as that experiment was done with a 50 mPa s oil [43,44]. See also Ref. [35] for other corrections. The last entries are also shown corrected with the measured 3% values of $l^*(0)$ and $l^*(90)$, and with the average time $\langle T_s \rangle$ spent in the slit added to T_{ch}.

Experiment	L mm	V_w (mm/s)	$\sqrt{2}d$ (mm)	$\gamma_F/(\gamma_F - \gamma)$	$M_e T_F V_w/\sqrt{2}d$	$l(0)/\sqrt{2}d$	$l(90)/\sqrt{2}d$	$R/l(0)$
Couder and Fort [2]	7.6	17.4	20.2	5–20	0.08–0.3	0.2–0.4	0.3–0.5	9–4
Andersen *et al.* [3]	5	15	14.1	21	0.5	0.9	1.0	7.3
Pucci *et al.* [6]	14.7	6.8	28.3	500	2.3	1.7	2.35	1.7
Ellegaard and Levinsen [7]	7.3	8.3	16.9	250	2.3	2.1	2.8	2.5
Ellegaard and Levinsen [7]	7.3	11.0	16.9	1000	12.5	2.5	4.3	2.2
Ellegaard and Levinsen [7]	5	11.1	13.7	1000	15.5	3.0	5.2	2.2
$b = 2$ mm barrier	5.2	9.8	14.0	500	6.7	2.8	4.4	2.3
$b = 2$ mm, corrected	5.2	9.8	14.0	500	5.4	1.0	3.1	6.0
$b = 0.5$ mm barrier	5.2	7.9	14.0	500	5.4	3.2	4.6	2.0
$b = 0.5$ mm, corrected	5.2	7.9	14.0	500	5.4	1.1	3.4	5.6

in this paper, and Figs. 7 and 11 in Ref. [7]), while for $b = 0.5$ mm we only see 1 or 2 crossings (Fig. 18). Finally, for the $L = 14.7$ mm slit we can have 1, 2, and 3 crossings at low values of V_w (Fig. 10, Ref. [7]), and 0, and 1 at high values of V_w (Fig. 23).

The explanation for these differences can be found in the wave height measurements by Rode *et al.* [23] (see Figs. 4, 5, and 6 in this reference). For the narrow $L = 5.2$ mm slit the extra damping, caused by the proximity of the boundaries when the drop visits the slit, leads to a decrease in the central peak, hence the drop in velocity. Also observed is an amplification of the wave amplitude in front of the drop (Figs. 4(a) and 4(b) in Ref. [23]). This leads to profound changes in the interaction for even small changes in, e.g., γ, D, h_1, or L as seen in the shift in symmetry, e.g., between Figs. 16 and 19 and for the 14.7 mm slit in Fig. 19, Ref. [7].

For the $L = 14.7$ mm slit the observed change is small at values of $M \leqslant 70$. Therefore, the angular response in this case mimics the angular response around a one-sided wall (Fig. 6, Ref. [6]), giving a preferred deflection angle as found by Pucci *et al.* [6]. However, the specific value depends on, e.g., h_1 and V_w.

As the Doppler shifted wave length in the wake depends on the velocity, the interaction with the corners behind after passage is rather complicated. For all values of L we find oscillating structures. Here the deflection angle sweeps back and forth as x_{imp} is moved monotonically across the slit i.e. the function $\alpha(x_{imp})$ is nonmonotonic. For an example, see Fig. 20(a). The actual response depends on the values of D, h_1, and γ, with maximum deflection angles found from $10°$ to nearly $70°$ for $L \leqslant 7.5$. For $M \geqslant 70$ we find oscillating structures also for the $L = 14.7$ mm slit while the limiting angle can be as low as $25°$ at high values of V_w (see Fig. 23). Such undetected oscillating structures were the main source of the seemingly chaotic response found by Pucci *et al.* [6].

Due to the complex interactions of the wave field with the slit and its environment, in reality all sizes of limiting angles are found. So the limiting angle of $60°$ is not generic as was assumed by Pucci *et al.* [6]. To get a better

understanding of these differences in response one would need many more wave field measurements. This is also the case for understanding the stop-and-go motion and resulting kinks for large numerical values of x_{imp}. But it is fair to assume, that the stop-and-go phenomenon, seen for instance in Fig. 16, is implicated in the complete stop seen at high drop velocities (i.e., for large drops).

D. Discussion

1. The velocity range

The information gained from the measurements on the wave field led us to reformulate the criteria proposed by Tadrist *et al.* [27]. These reformulated criteria were then used to evaluate the optimal regime for possibly observing true interference. This regime was already mostly covered by our previous investigation [7]. However, the extra time used by the drop while inside the slit was not taken into account in calculating the normalized damping time τ_D. This suggested that the optimum velocity range for the slits used would be somewhat higher, prompting us to investigate the complete range of high-velocity walkers. Independence of α on x_{imp}, as pointed out by Pucci *et al.* [6], could be caused by the chaotic bouncing of drops at low velocities leading to quantumlike behavior. This might thus be seen already in the single-slit case. The investigation was therefore also extended towards the low velocity boundary for walkers.

Here a low velocity boundary was found for all slit sizes. Close to the boundary we found that the structure of the ensemble of trajectories is the same for all slits. An example is shown in Sec. IV A, Fig. 13. Therefore, it is natural to assume that a single mechanism lies behind. We notice that the slit system seems to act as a potential barrier for a single object. This is supported by the limit dropping from about 8 mm/s for a $b = 5$ mm barrier to below 6 mm/s for a $b = 0.5$ mm barrier while keeping the fluid height constant. As the slit is much wider than the drop and much narrower than the extent of the wave field close to the critical drive amplitude, the passage of the drop is governed by the kinetic energy of this

combination, as defined in Ref. [41]. Thus, here we have an analogy to quantum theory, where a bare particle becomes dressed through interaction with excitations of a field. However, no sign of chaotic behavior or true interference was found at all.

The theoretical prediction was that high drop velocity most likely was needed to observe true interference in a double-slit, but an investigation of this regime did not find any sign of this. Nor was any sign of chaotic behavior detected in single-slits.

A curious phenomenon was observed both in the single- and in the double-slit case. When the impact velocity is increased beyond a critical value, a transition region is entered. In this, the window in x_{imp} occupied by regular trajectories disappears very fast with one or more forbidden zones appearing, inside which no regular trajectories exist. The extent of this transition region is roughly represented by the orange cross-hatched rectangle in the upper right corner of the (Ω, γ) parameter space in Fig. 1.

The transition region is seen to overlap with the stable $(2,1)$ and $(2,1)^2$ walking modes. As noted by Wind-Willassen *et al.* [22], stationary chaotic bouncing drops in the regime around $\Omega = 1$ could, when pushed, change state into a stable walking mode. As our drops start out with a finite velocity due to the horizontal drop maker, these drops can perform the opposite transition into the stationary chaotic bouncing mode. A similar transition into a stationary state is seen in this regime, if the drive is lowered and then reset while the drop is far from boundaries. We should note here that the upper limiting velocity for walkers reported here corresponds well with the upper limit for walkers reported in Ref. [42].

2. Double-slit

Finally, we consider the double-slit case. Compared to our previous investigation [7] we also use barriers with smaller values of b ($b = 2$ and 0.5 mm) to limit the time used to transit the barrier. Again we find an upper limit to the velocity for passage of the drops. However, even in the transition region, where the forbidden zones develop, all regular trajectories show a fully dependent relation between the angular deflection and the impact parameter.

The extra interference found for the double-slit as compared to the single-slit is still present. Also here, it is found to be caused by back-reflection of waves after passage at all velocities, where passage of the slits is possible. This conclusion is backed by the behavior of high velocity drops crossing the barrier comparatively close to the slits in the case of the $b = 0.5$ mm barrier for values of $h_1 \gtrsim 0.8$ mm (Fig. 24). Furthermore, since drops following irregular trajectories are simply caught dead in their tracks, no support for a chaotic or quantumlike behavior is found here either.

In Table II we give a summary of the experiments done so far on the double-slit system.

In the last entries we have used the measured values for $l^*(0)$ and $l^*(90)$ together with the average time $\langle T_s \rangle$ spent in the slit added to the characteristic time T_{ch}. While the change in the normalized damping time clearly can be minimized by using barriers with b as small as 0.5 mm, it is quite impossible to meet the spatial criteria even using the rather liberal values of $l^*(0)$ or $l^*(90)$.

To round off the discussion, the orange bordered rectangle to the right side of Fig. 1 shows the range of the parameter space now investigated in detail in this paper and in Ref. [7] for $L = 5.2$, 7.5, and 14.7 mm. This covers the complete range of velocities of walkers for which it is possible to pass a slit opening with L equal to the sizes considered here.

V. CONCLUSIONS

The idea of using bouncing drops as a proxy for quantum systems is truly fascinating. But the intriguing observation, that the true interference patterns of a quantum mechanical double-slit was reproduced with walking drops [2], has since been proven wrong by several authors [3,6,7]. Still, that randomness could be caused by chaotic bouncing was yet an open question [6,45].

In earlier experiments with walking drops interacting with slits less than half of the available phase space for walkers at high γ have been investigated (the hatched region in Fig. 1). Here we report new experiments covering the complete phase space where we search for true interference and for randomness induced by chaotic bouncing.

A main criterion for the possibility of true interference is that the accompanying wave field, passing through the slit not traversed by the drop, reaches the other side soon enough and with sufficient amplitude to have a significant impact. A novel insight in this aspect is obtained through measurements presented here on the damping of the wave field in both space and time. This was done for drive values up to extremely close to the spontaneous onset of Faraday waves. Recently, Tadrist *et al.* [27] formulated simple criteria for possible true interference based on a theoretical derivation of the accompanying wave field. We find very good agreement with their theory in its full form. However, due to discrepancies caused by a simplification used to derive the criteria, we have reformulated these based on the full theory.

While the criteria can only be considered as guidelines in pinning down regions of interest, they do highlight that the time spent inside the slit should be minimized. In a major step forward in the search we have therefore repeated this with ultra-thin barriers down to a breadth b of 0.5 mm. Thus, we have now systematically covered the whole possible regime for slits with b equal to 5, 2, and 0.5mm. This regime is indicated in Fig. 1 by the large orange bordered rectangle to the right.

But in all cases we still find that—within very small experimental uncertainties–the movements are always truly dependent and without any sign of true interference or chaos.

The investigation has also led to further insight in the interaction of both small and large drops with slits.

As drops are made smaller we find a low velocity limit. The structure of the ensemble of trajectories is found to be the same for all slit sizes L with the velocity limit going down as L becomes wider or the fluid height or γ is increased. Thus, the slit system seems to act as a potential barrier.

For large drops we also find a limiting velocity. This depends on the slit size but is rather independent of γ. Decreasing b results in a small increase in the limiting velocity as the barrier becomes less effective in damping the waves. Drops following irregular trajectories still make it through the
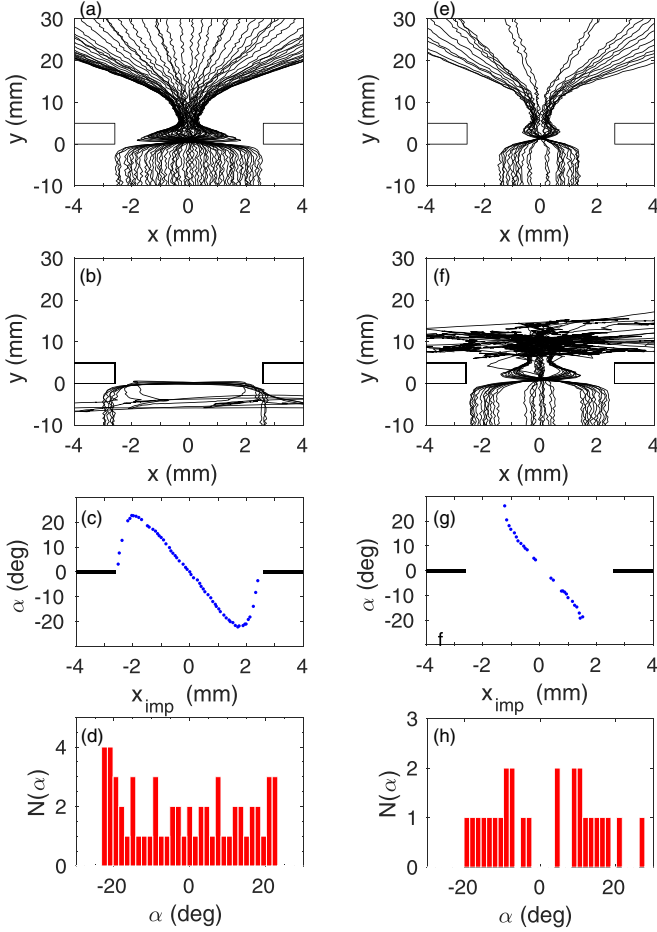
FIG. 21. $L = 5.2$ mm, $b = 5$ mm. In the left column we show the result for drops moving with impact velocity $V_w = 14.10 \pm 0.04$ mm/s and $D = 0.838 \pm 0.016$ mm, while in the right column we present the result for drops with impact velocity $V_w = 15.01 \pm 0.10$ mm/s and $D = 0.870 \pm 0.016$ mm. Sweeping the impact parameter, panels (a) and (e) show regular trajectories for drops that pass into the far region, (b) and (f) trajectories of those that do not make it further than the local neighborhood at the outlet of the slit. Notice the expanded x-scale. Panels (c) and (g) shows the associated (x_{imp}, α) plots with the line segments at $\alpha = 0$ symbolizing the barrier with slit opening. $h_1 = 0.650 \pm 0.040$ mm and $\gamma/\gamma_F = 0.991 \pm 0.001$. At a velocity of $V_w = 15.76 \pm 0.03$ mm/s and $D = 0.901 \pm 0.020$ mm, no drops make it through the slit without coming to a complete stop after which most drift around slowly close to the outlet of the slit. (d), (h) Histograms of the corresponding angular distributions.

slit. But now stop and stay close to the outlet thus calling for a different explanation, most likely a combination of the wave field interacting with the barrier, and that in this regime moving drops can coexist with stationary drops [22].

We have also displayed histograms of the distribution of angular response. While a single histogram for a double-slit [Fig. 20(c)] looks somewhat like the quantum mechanical equivalent, the most striking observation is how similar the histograms can look for quite different angular responses.

The walker-slit interaction is a complex hydrodynamic problem, and interesting in itself. But our main conclusion
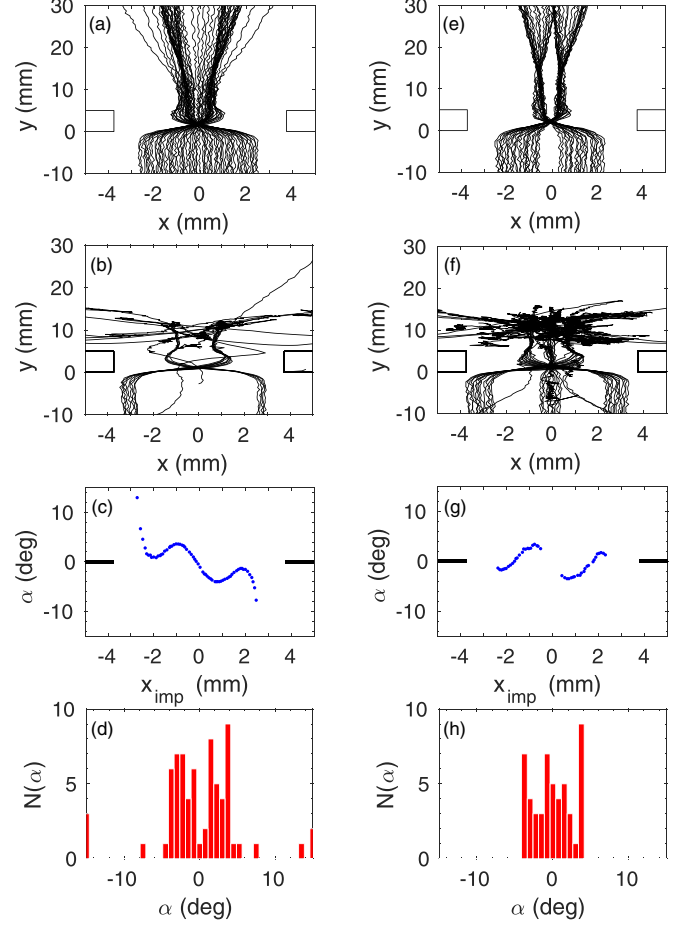
FIG. 22. $L = 7.5$ mm, $b = 5$ mm. In the left column we show (a) the regular trajectories of the drops moving with an impact velocity $V_w = 15.17 \pm 0.04$ mm/s and $D = 0.881 \pm 0.015$ mm, (b) those that do not make it further than the local neighborhood of the slit together with some of the backtracking trajectories, (c) the associated (x_{imp}, α) plot. Again the x axis is expanded. (d) Histogram of the angular distribution. In the right column (e)–(h) the same is shown for drops of a velocity of $V_w = 15.62 \pm 0.03$ and $D = 0.892 \pm 0.15$ mm. $\gamma/\gamma_F = 0.998$ and $h_1 = 0.630 \pm 0.040$ mm. At a velocity of $V_w = 15.84 \pm 0.05$ mm/s no drops make it through the slit without coming to a complete stop. The line segments in panels (c) and (g) at $\alpha = 0$ symbolize the barrier with slit opening.

is still: There are many quantumlike phenomena in the drop systems, notably quantized orbits of interacting drops, and, e.g., the notion of dressed mass, but nowhere is found the genuine fortuitousness characteristic of quantum physics [46].

APPENDIX A: HIGH VELOCITY REGIME

Here we present some results for the different single-slits in Fig. 21 ($L = 5.2$ mm), Fig. 22 ($L = 7.5$ mm), and Fig. 23 ($L = 14.7$ mm). These results are obtained just below and inside the transition region in the high velocity regime.

The figures display the regular trajectories, the irregular trajectories and the angular response, and illustrate both differences and common features. As seen, even in the transition region the angular response is always truly dependent without any sign of chaos: The distributions are symmetric and reproducible.
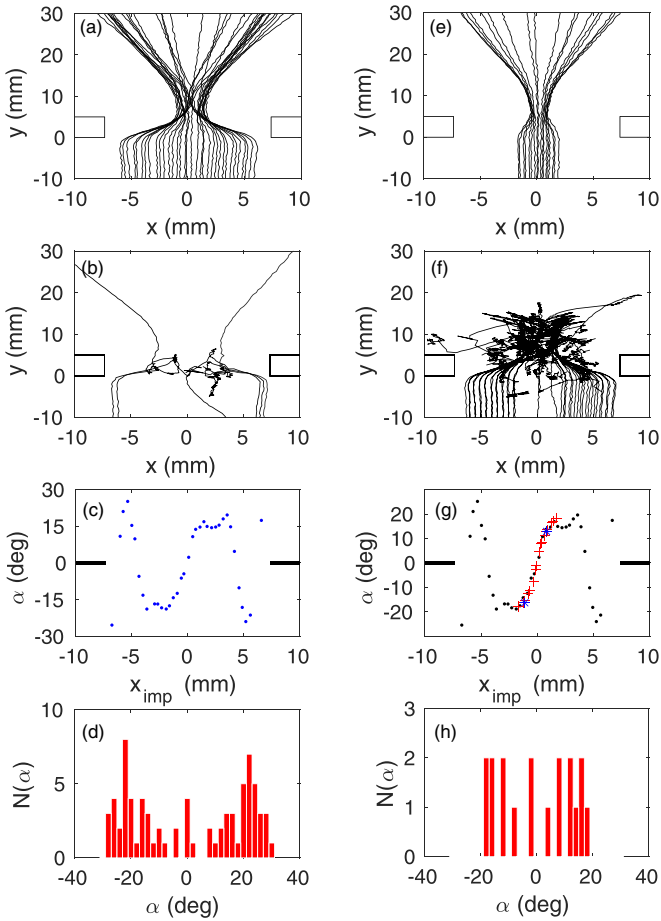

FIG. 23. $L = 14.7$ mm, $b = 5$ mm. In the left column we show (a) the regular trajectories of the drops moving with an impact velocity $V_w = 15.86 \pm 0.03$ mm/s and $D = 0.887 \pm 0.020$ mm that pass into the far region, (b) some irregular trajectories surrounding the regular trajectories, (c) the associated (x_{imp}, α) plot. Notice again the expanded x axis. (d) Histogram of the angular distribution. In the right column the same is shown for drops of a velocity of $V_w = 16.31 \pm 0.03$ (+) and $D = 0.920 \pm 0.020$ mm. Superimposed on the (x_{imp}, α) plot (g) are the data from the left column ($\cdot$), and data for a drop having $V_w = 16.42$ mm/s and $D = 0.931 \pm 0.020$ mm ($*$). $\gamma/\gamma_F = 0.998$ and $h_1 = 0.550 \pm 0.040$ mm. At a velocity higher than $V_w = 16.42 \pm 0.05$ mm/s no drops make it through the slit without coming to a complete stop. The line segments in panels (c) and (g) at $\alpha = 0$ symbolize the barrier with slit opening.

APPENDIX B: TUNNELING

In Fig. 24 we show an example of the barrier crossing mentioned in Sec. IV C 2. The example shown is for a single-slit having $L = 5.2$ mm and $b = 0.5$ mm. Compared to Fig. 17 it is clear that the behavior of trajectories that pass inside the slit is very similar in the two cases while outside the slit the trajectories gradually revert to passing undisturbed. As h_1 is lowered, the trajectories passing over the barrier close to the slit start bending towards the slit and no longer pass and finally also the straight trajectories far from the barrier are reflected. It is interesting that as soon as the influence of the slit on the incoming drop has disappeared, the outgoing part of the trajectory is unaffected by the slit.

This happens already at a distance of 10 mm from the center of the slit. Taking this distance as d gives $l_D^*(0) \sim 1$ and $l_D^*(90) \sim 3$ whether taking the theoretical 3% values or the measured values.
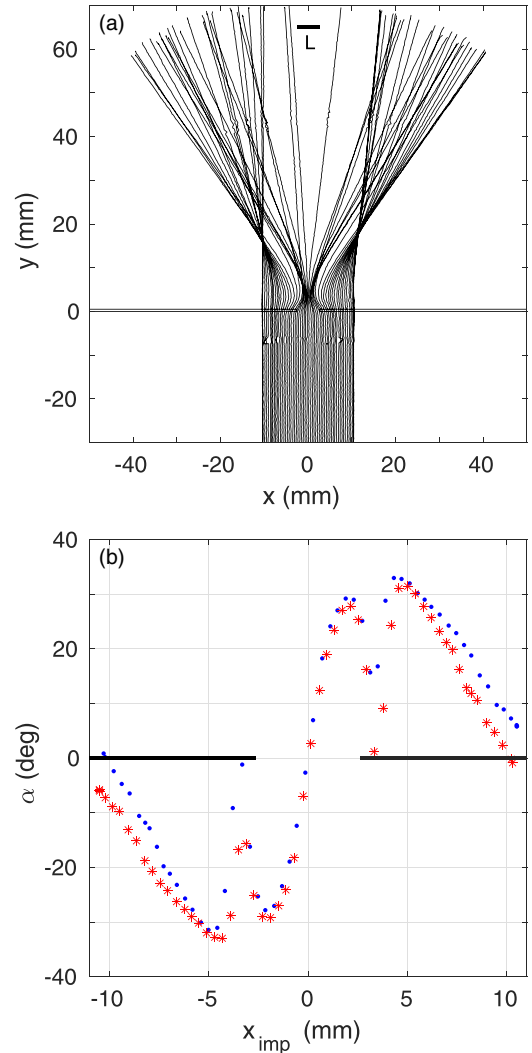

FIG. 24. Single-slit, $L = 5.2$ mm, $b = 0.5$ mm, 57 trajectories, $h_1 = 0.950 \pm 0.040$ mm, $\gamma/\gamma_F = 0.992 \pm 0.001$, $V_w = 10.06 \pm 0.06$ mm/s, and $D = 0.810 \pm 0.014$ mm. (a) Trajectories, (b) α versus x_{imp} ($\cdot$). Point symmetric copy ($*$). The line segments at $\alpha = 0$ symbolize the barrier with the slit.

[1] Y. Couder, S. Protiére, E. Fort, and A. Boudaoud, Walking and orbiting droplets, Nature (London) **437**, 208 (2005).

[2] Y. Couder and E. Fort, Single-particle diffraction and interference at a macroscopic scale, Phys. Rev. Lett. **97**, 154101 (2006).

[3] A. Andersen, J. Madsen, C. Reichelt, S. Rosenlund Ahl, B. Lautrup, C. Ellegaard, M. T. Levinsen, and T. Bohr, Double-slit experiment with single wave-driven particles and its relation to quantum mechanics, Phys. Rev. E **92**, 013006 (2015).

[4] T. Bohr, A. Andersen, and B. Lautrup, Bouncing droplets, pilot-waves, and quantum mechanics, in *Recent Advances in Fluid Dynamics with Environmental Applications*, edited by J. Klapp, L. D. G. Sigalotti, A. López, and Ruiz-Chavarria (Springer International Publishing, Berlin, 2016), pp. 335–349.

[5] H. Batelaan, E. Jones, W. Cheng-Wei Huang, and R. Bach, Momentum exchange in the electron double-slit experiment, J. Phys.: Conf. Ser. **701**, 012007 (2016).

[6] G. Pucci, D. M. Harris, L. M. Faria, and J. W. M. Bush, Walking droplets interacting with single and double slits, J. Fluid Mech. **835**, 1136 (2018).

[7] C. Ellegaard and M. T. Levinsen, Interaction of wave-driven particles with slit structures, Phys. Rev. E **102**, 023115 (2020).

[8] S. Protière, A. Boudaoud, and Y. Couder, Particle-wave association on a fluid interface, J. Fluid Mech. **554**, 85 (2006).

[9] S. Protière, S. Bohn, and Y. Couder, Exotic orbits of two interacting wave sources, Phys. Rev. E **78**, 036204 (2008).

[10] M. Labousse, S. Perrard, Y. Couder, and E. Fort, Self-attraction into spinning eigenstates of a mobile wave source by its emission back-reaction, Phys. Rev. E **94**, 042224 (2016).

[11] S. Perrard and M. Labousse, Transition to chaos in wave memory dynamics in a harmonic well: Deterministic and noise-driven behavior, Chaos **28**, 096109 (2018).

[12] A. Eddi, E. Fort, F. Moisy, and Y. Couder, Unpredictable tunneling of a classical wave-particle association, Phys. Rev. Lett. **102**, 240401 (2009).

[13] A. Nachbin, P. A. Milewski, and J. W. M. Bush, Tunneling with a hydrodynamic pilot-wave model, Phys. Rev. Fluids **2**, 034801 (2017).

[14] L. Tadrist, T. Gilet, P. Schlagheck, and J. W. M. Bush, Predictability in a hydrodynamic pilot-wave system: Resolution of walker tunneling, Phys. Rev. E **102**, 013104 (2020).

[15] D. M. Harris, J. Moukhtar, E. Fort, Y. Couder, and J. W. M. Bush, Wavelike statistics from pilot-wave dynamics in a circular corral, Phys. Rev. E **88**, 011001(R) (2013).

[16] T. Gilet, Dynamics and statistics of wave-particle interactions in a confined geometry, Phys. Rev. E **90**, 052917 (2014).

[17] T. Gilet, Quantumlike statistics of deterministic wave-particle interactions in a circular cavity, Phys. Rev. E **93**, 042202 (2016).

[18] T. Cristea-Platon, P. J. Sáenz, and J. W. M. Bush, Walking droplets in a circular corral: Quantization and chaos, Chaos **28**, 096116 (2018).

[19] D. M. Harris, P.-T. Brun, A. Damiano, L. Faria, and J. W. M. Bush, The interaction of a walking droplet and a submerged pillar: From scattering to the logarithmic spiral, Chaos **28**, 096105 (2018).

[20] J. W. M. Bush and A. U. Oza, Hydrodynamic quantum analogs, Rep. Prog. Phys. **84**, 017001 (2021).

[21] M. Faraday, On the forms and states assumed by fluids in contact with vibrating elastic surfaces, Phil. Trans. R. Soc. Lond. **121**, 319 (1831) (Appendix to: On a peculiar class of acoustical figures; and on certain forms assumed by groups of particles upon vibrating elastic surfaces, *ibid.* p. 299).

[22] Ø. Wind-Willassen, J. Moláček, D. M. Harris, and J. W. M. Bush, Exotic states of bouncing and walking droplets, Phys. Fluids **25**, 082002 (2013).

[23] M. Rode, J. Madsen, and A. Andersen, Wave fields in double-slit experiments with wave-driven droplets, Phys. Rev. Fluids **4**, 104801 (2019).

[24] R. Dubertrand, M. Hubert, P. Schlagheck, N. Vandewalle, T. Bastin, and J. Martin, Scattering theory of walking droplets in the presence of obstacles, New J. Phys. **18**, 113037 (2016).

[25] L. M. Faria, A model for Faraday pilot waves over variable topography, J. Fluid Mech. **811**, 51 (2017).

[26] M. Durey and P. A. Milewski, Faraday wave-droplet dynamics: Discrete-time analysis, J. Fluid Mech. **821**, 296 (2017).

[27] L. Tadrist, J.-B. Shim, T. Gilet, and P. Schlagheck, Faraday instability and subthreshold Faraday waves: Surface waves emitted by walkers, J. Fluid Mech. **848**, 906 (2018).

[28] In Ref. [7] we compared our drop size measurements with those of other authors in the field and found that on average our measurement was 4% too low (see Ref. [7], Fig. 2). As the velocity close to γ_F can be measured much more precisely, we used this to characterize the drops used there.

[29] T. B. Benjamin and F. Ursell, The stability of the plane free surface of a liquid in vertical periodic motion, Proc. R. Soc. London A **225**, 505 (1954).

[30] A. Eddi, E. Sultan, J. Mouktar, E. Fort, M. Rossi, and Y. Couder, Information stored in Faraday waves: The origin of a path memory, J. Fluid Mech. **674**, 433 (2011).

[31] J. Moláček and J. W. M. Bush, Drops walking on a vibrating bath: Towards a hydrodynamic pilot-wave theory, J. Fluid Mech. **727**, 612 (2013).

[32] F. Blanchette, Modeling the vertical motion of drops bouncing on a bounded fluid reservoir, Phys. Fluids **28**, 032104 (2016).

[33] K. Kumar, and L. Tuckerman, Parametric instability of the interface between two fluids, J. Fluid Mech. **279**, 49 (1994).

[34] H. W. Müller, H. Wittmer, C. Wagner, J. Albers, and K. Knorr, Analytic stability theory for Faraday waves and the observation of the harmonic surface response, Phys. Rev. Lett. **78**, 2357 (1997).

[35] The correct value of D_{diff} used in Eq. (2.60), Ref. [27], is 2.20 mm^2 as stated in their Table 1, not 4.40 mm^2 as given below Eq. (2.66).

[36] A. P. Damiano, P.-T. Brun, D. M. Harris, C. A. Galeano-Rios, and J. W. M. Bush, Surface topography measurements of the bouncing droplet experiment, Exp Fluids **57**, 163 (2016).

[37] We only show the combined statistical error on M stemming from γ and γ_F. Due to the strict temperature control of the bath, the variation on the physical value of γ_F is negligible, and we use the most likely value for γ_F. The error on γ_F is dominated by the systematic error of $\pm 0.06\%$. This amounts to a, albeit nonlinear, scaling of the M-axis, that fortunately leaves the part of the plot for $M \leqslant 100$ essentially unchanged.

[38] The 3% contour line only depends on the shape of the wave field, not the actual size. As the measured value is at fixed absolute size, the close agreement means that the absolute size of the waves is nearly constant in the memory regime where V_w is constant.

[39] B. Lautrup, *Physics of Continuous Matter* (IOP Publishing Ltd, Bristol, UK, 2005).

[40] If a neighborhood exists around every point of a curve such that the curve can be graphed by a differentiable function, then the curve is defined as smooth mathematically. If the curve has a kink, then a singular point exists, where the first derivative is not defined. A cusp is a kink, where the first derivative reverses direction.

[41] J. W. M. Bush, A. U. Oza, and J. Moláček, The wave-induced added mass of walking droplets, J. Fluid Mech. **755**, R7 (2014).

[42] S. Protiéere, Gouttes rebondissantes: une association onde-particule à échelle macroscopique, Ph.D. Thesis, L'Université Paris-Diderot (Paris VII), France (2007).

[43] A. Eddi, Marcheurs, dualité onde-particule et mémoire de chemin., Ph.D. Thesis, L'Université Paris-Diderot (Paris VII), France (2011).

[44] https://www.dow.com/en-us/pdp.xiameter-pmx-200-silicone-fluid-05-cst.01013181z, properties at 25°: XIAMETER PMX-200 Silicone Fluid 50 mPa s.

[45] Tadrist *et al.* [27] suggested that true interference might be observable at lower viscosity fluids. However, based on simulations we sincerely doubt this. Still this does not exclude the possibility that by using a lower viscosity fluid, chaotic bouncing might result in a chaotic response from a single-slit.

[46] A. Bohr and O. Ulfbeck, Primary manifestation of symmetry. Origin of quantal indeterminacy, Rev. Mod. Phys. **67**, 1 (1995); Ole Ulfbeck and Aage Bohr, Genuine fortuitousness: Where did that click come from? Found. Phys. **31**, 757 (2001).